Taylor & Francis
Taylor & Francis Group

🔓 OPEN ACCESS | Check for updates

Neural network-based regression for heat transfer and fluid flow over in-line cylinder arrays with random pitch distances at low Reynolds number

Geunhyeok Choi[a,b], Seong Jin Kim[b] and Seungwon Shin [ID][a]

[a]Department of Mechanical and System Design Engineering, Hongik University, Seoul, Republic of Korea; [b]Extreme Materials Research Center, Korea Institute of Science and Technology, Seoul, Republic of Korea

ABSTRACT

Finding an arrangement, leading to a higher heat transfer and lower pressure drop, is crucial in the design of heat exchangers. Previous studies have primarily focused on regular arrangements with uniform pitch distances, which lack applicability to general configurations. In this study, we proposed a new procedure of a flow-learned building block (FLBB) to predict heat transfer in an in-line cylinder array with random pitch distances using a neural network-based regression analysis with a systematic data generation process. As a first step, we demonstrated the FLBB's capability to predict the heat transfer and pressure drop in in-line cylinder arrays with random pitch distances at low Reynolds numbers from 1 to 100 for air ($Pr = 0.71$). Subsequently, a high-order FLBB approach was proposed to address the spatial interdependency between neighbouring cylinders, particularly in scenarios where vortex shedding occurs in the wake of cylinders at increased Reynolds numbers. The high-order FLBB approach was then shown to successfully describe various flow and temperature patterns using cylinder arrays with random pitch distances. The proposed procedure exhibited remarkable efficiency, requiring only about 1 s. Furthermore, the FLBB was successfully extended to various flow regimes, even encompassing unseen Reynolds numbers from 1 to 100.

Nomenclature

A	surface area, m^2
c	specific heat capacity, J/(kg·K)
C_d	drag coefficient
C_f	skin-friction coefficient
C_p	pressure coefficient
D	cylinder diameter, m
h	convection heat transfer coefficient, W/(m^2·K)
k	thermal conductivity, W/(m·K)
L_2 L_2	norm error
L_∞	infinity norm error
Nu	Nusselt number
$\dot{m}$	mass flow rate, kg/s
p	pressure, Pa
Δp	pressure drop, Pa
$\Delta p*$	normalised pressure drop
Pr	Prandtl number
Q	heat transfer rate, W
Re	Reynolds number
S_L	longitudinal pitch distance, m
S_T	transverse pitch distance, m
T	temperature, K
ΔT_{LMTD}	logarithmic mean temperature difference, K
t	time, s
U	bulk velocity, m/s
u	horizontal velocity, m/s
$u*$	normalised horizontal velocity
v	vertical velocity, m/s
$v*$	normalised vertical velocity

Greek letters

μ	viscosity, Pa·s
ρ	density, kg/m^3
θ	normalised temperature
ω	vorticity, 1/s
$\omega*$	normalised vorticity

CONTACT Seong Jin Kim ✉ kyk756@kist.re.kr; Seungwon Shin ✉ sshin@hongik.ac.kr 🏛 Hongik University, Seoul, 04066, Republic of Korea

Subscripts

in   inlet
out   outlet
max   maximum

1. Introduction

Heat transfer and fluid flow through cylinder arrays is a fundamental subject in thermal and fluid engineering and has direct implications in a wide variety of applications such as heat exchangers (Colburn, 1993; da Silva et al., 2018; Ge et al., 2021; Zargartalebi et al., 2020; Zukauskas & Ulinskas, 1988), particulate filters (Araujo et al., 2006; Li et al., 2016; Printsypar et al., 2019), gas diffusion layers (Cindrella et al., 2009; Tamayol & Bahrami, 2011; Williams et al., 2004), and packed bed reactors (Halkarni et al., 2017; Nemec & Levec, 2005; Noorman et al., 2007). Because the performance of these applications is determined by the flow characteristics near the solid surface, the geometric configuration of the cylinder array should be designed to induce optimal fluid flow for each purpose (Gorman et al., 2019; Li et al., 2016). For example, enhancing convective heat transfer by inducing local turbulence or vortex flow has long been a topic of interest for heat exchangers (da Silva et al., 2018). To date, numerous studies have been conducted to determine the boundary conditions and optimal geometric features, such as the pitch distance, in-line/staggered composition of cylinder arrays, and shape and size of cylinder, for different applications (Ge et al., 2021; Li et al., 2016).

Most earlier studies have focused on flows over arrangements of cylinders of the same size, ranging from millimetres to metres (Colburn, 1993; da Silva et al., 2018; Zukauskas & Ulinskas, 1988). The flow regimes in these studies predominantly fell within the fully turbulent (Dhar et al., 2016, 2017) or transition regions. In these studies, uniformly arranged in-line and staggered patterns were commonly utilised, characterised by their longitudinal and transverse pitch distances and sizes. These parameters have a significant influence on flow behaviour and heat transfer performance. Additionally, numerous studies have been conducted to identify the optimised arrangements that can minimise the pressure drop while simultaneously achieving an enhanced heat-transfer performance. The research outcomes were utilised to determine correlations between the Nusselt number Nu (representing the heat transfer performance), pressure drop (representing the required pump power), Reynolds number Re, and Prandtl number Pr depending on the geometric parameters (Colburn, 1993; Grimison, 1937; Zukauskas & Ulinskas, 1988).

Recently, there has been a notable increase in research focusing on the flow over cylinder arrays at the sub-micro- and microscale (He & Zhang, 2020; Jiang et al., 2014; Zargartalebi & Azaiez, 2019; Zargartalebi et al., 2020). Specifically, studies were conducted on systems such as microchannel heat sinks (Zargartalebi & Azaiez, 2019; Zargartalebi et al., 2020) and mass separation (He & Zhang, 2020; Jiang et al., 2014). In these configurations, low Reynolds-number flows, ranging from the order of tens to several hundred (He & Zhang, 2020; Zargartalebi & Azaiez, 2019; Zargartalebi et al., 2020), and even creeping flow ($Re \ll 1$) (Chen & Papathanasiou, 2008; He & Zhang, 2020), were employed. The configurations of these systems can sometimes become significantly complex owing to the presence of a large number of cylinders with nonuniform distributions (Chen & Papathanasiou, 2008; He & Zhang, 2020). In the context of designing optimised structures that aim to reduce the pressure drop while maintaining higher heat transfer coefficients, previous research has explored specific geometric configurations by employing different pitch distances, sizes, and shapes. To attain these desired objectives, researchers have employed disordered or heterogeneous arrays and conducted performance comparisons with regular in-line or staggered arrays (Zargartalebi et al., 2020). These studies have revealed that well-designed heterogeneous arrays featuring varying pitch distances or sizes can occasionally outperform homogeneous arrays by enhancing the heat transfer efficiency. However, these study findings cannot be readily extended to general geometries depending on the user's available options. Owing to the extensive range of cylinders that can be employed in such systems, the number of potential configurations is virtually limitless. Consequently, identifying the optimal configuration is impractical. Therefore, establishing a correlation to predict the overall heat transfer and pressure drop in a given system is crucial for initial system design assessment. This correlation would streamline the design process, enabling the efficient exploration of various configurations and the identification of promising designs without relying solely on resource-intensive experimental trials. However, most existing correlations for heat transfer have been limited to homogeneous arrays with uniform size and pitch. A more general correlation that can encompass heterogeneous arrays cannot be easily determined using conventional approaches due to its case-specific nature. From this research gap, we have devised a new and innovative tool for addressing fluid flow and heat transfer over a further general geometric configuration of cylinder arrays with heterogeneity. To achieve this research objective to obtain a more general correlation, we have incorporated a machine learning process.

The recent advances in machine learning (ML) have provided new perspectives for delivering quantified solutions from vast datasets using computational resources or experimental measurements. ML approaches have also been used in the fields of thermal and fluid mechanics (Brunton et al., 2020; Duraisamy et al., 2019; Han et al., 2022; Jin et al., 2018, 2021; Kutz et al., 2016; Lee & You, 2019; Ling et al., 2016; Raissi et al., 2017, 2019, 2020; Schmid, 2010; Wang et al., 2017; Wu et al., 2020; Zhang et al., 2022; Zhou et al., 2019), which have an inherently nonlinear nature, adding difficulties in predicting and/or describing the temporal and spatial evolutions of flow fields. A representative topic in conventional ML is the regression analysis (Acharya et al., 2019; Chew & Law, 2019; Maulud & Abdulazeez, 2020; Wang & Sun, 2016; Zhang et al., 2019), which refers to a method that correlates independent and dependent variables. Using regression analysis, a large number of input conditions, which are impossible to correlate with a theoretical or mathematical model, can be successfully correlated without any physical support. Owing to the advancement of the computational fluid dynamics (CFD) analysis, the available dataset for training has become sufficiently large; however, it is still limited to target problems with specific geometric configurations. Therefore, a systematic procedure with a practically obtainable data generation process is required to implement a CFD analysis.

In this study, we introduce a new methodology to predict fluid flow and heat transfer over in-line cylinder arrays including heterogeneity in its pitch distance, using a neural network-based regression analysis (Acharya et al., 2019; Chew & Law, 2019; Maulud & Abdulazeez, 2020; Wang & Sun, 2016; Zhang et al., 2019) with a systematic and automatic data generation method. As a critical first step for the future design of thermal and fluid engineering applications with cylinder arrays, the present work suggests a novel procedure called flow-learned building block (FLBB) approach. The FLBB discretizes the whole flow domain into subblocks and learns all the systematic flow data that are possible in the subblocks. Because a subblock may or may not have cylinder, building subblocks in different combinations can yield possible flow patterns over cylinder arrays with random pitch distances. To verify the performance of the FLBB proposed in this study, we employed low Reynolds flows over in-line cylinder arrays, which are one of the most widely used configurations in heat exchangers, and compare the results predicted by the FLBB to the target data regarding geometric cases and flow regimes.

2. Methods

2.1. Flow-learned building block

As stated before, there is currently only one case-specific method to describe fluid flow over heterogeneous arrays, owing to the nonlinear flow characteristics that change depending on the geometric configurations (Henderson, 1997). Many nonlinear mechanics problems have been successfully solved using computational approaches that linearise them, such as the finite element and finite volume methods, which discretize the spatial and temporal domains into linear subunits. In these methods, the minimal spatial subunit obtained by discretizing the spatial domain, which is usually referred to as a computation mesh or grid, plays an important role in solving nonlinear mechanical problems.

This discretization of the spatial and temporal domains into small subunits in various computational approaches motivated the development of the FLBB. Instead of defining a subunit as a sufficiently small region for linearisation, a large building block comprising cylinder arrays with random pitch distances is considered. The size of the building block was set as the transverse distance (S_T) between the circular cylinders, as shown in Figure 1(a), which illustrates the longitudinal heterogeneity of the cylinder array. Notably, in most cylinder arrays used in fluid engineering (e.g. heat exchangers), heterogeneity in the longitudinal direction, rather than in the transverse direction, is considered much more important because it causes heterogeneity in the flow direction (Lee et al., 2013; Li et al., 2016). Therefore, although exploring transverse heterogeneity and arbitrarily shaped cylinders is one of our long-term goals, in this first study, we focused on longitudinal heterogeneity. Figure 1(a) shows that longitudinal heterogeneity is imposed by a building block that is void of a cylinder. The two types of building blocks were: void and filled. The void building blocks did not contain a cylinder, whereas the filled building blocks did contain a cylinder. Subsequently, numerous sets of longitudinal heterogeneous arrays were configured by arbitrarily combining these void and filled building blocks. The dotted box in Figure 1(a) denotes a heterogeneous unit arrangement in the longitudinal direction, where periodic boundary conditions are applied along the transverse direction. The definition of an FLBB is a building block that has learned about the flow patterns across discretized subblocks in response to geometric conditions based on the void and filled building blocks. The flow pattern across subblocks was learned using a data-based function approximator neural network (NN), which is suitable for handling various patterns of complex
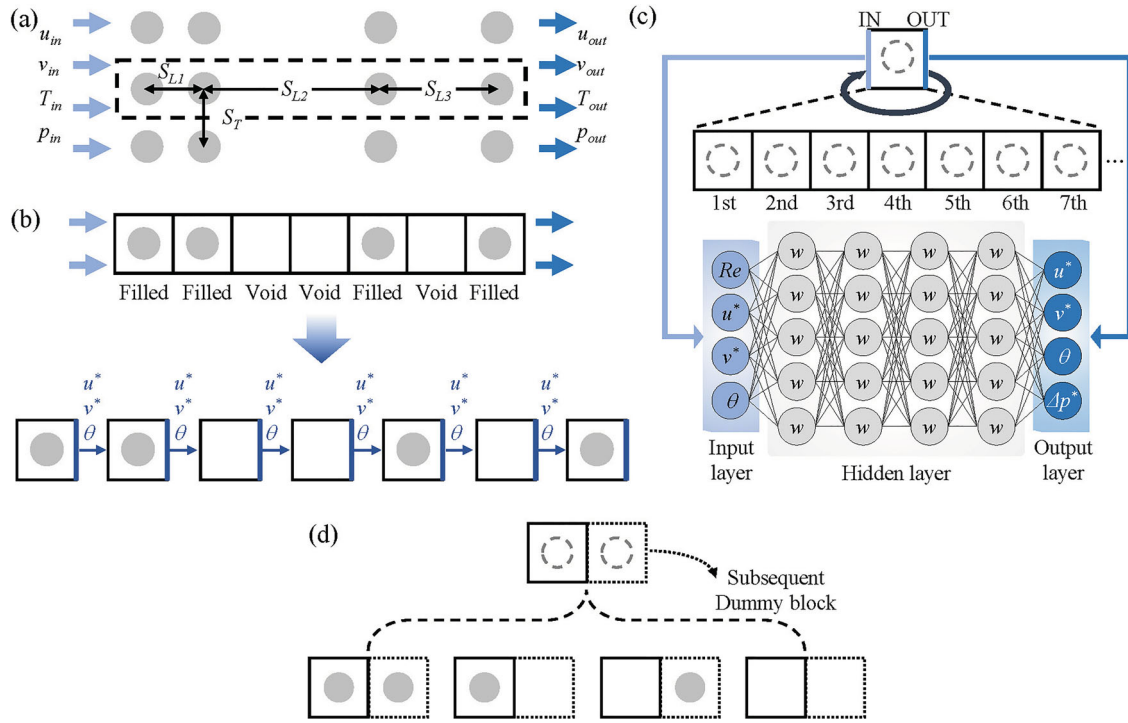
Figure 1. Flow-learned building block approach. (a) The heterogeneous flow domain with periodicity along the transverse direction (b) The basic concept of FLBB is to discretize target flow domain along the flow direction (c) The recursive data generation procedure and neural network (NN) architecture for the FLBB. (d) Second-order FLBB approach by introducing the subsequent dummy block.

problems (Brunton et al., 2020). After flow pattern learning, the NN was used to predict the flow distribution at the right outlet boundary for various flows arriving at the left inlet boundary of the subsequent block; in this study, the flow was set to flow from left to right. The predicted flow pattern at the right outlet boundary of this building block was then used as an inflow condition at the inlet boundary of the next building block on the right. In this sequence, the flow distribution over the entire cylinder array can be predicted, as shown in Figure 1(b).

To improve the generalisation ability of the NN, which refers to the predictability of the untrained data obtained using an ML technique, a wide range of flow patterns must be included in the NN dataset (Xu & Mannor, 2012). One of the significant challenges in setting up an NN dataset is ensure that all possible flow patterns that can occur in heterogeneous cylinder arrays are included. For this purpose, a recursive data generation process was devised, as shown in Figure 1(c). In Figure 1(c), the dashed circular lines in the black boxes represent void or filled building blocks. During the first data generation, or the first layer, an initial uniform fluid flow was introduced at the left inlet boundary of a training domain with or without a cylinder (void or filled). The time-variant data of $u(y, t)$ and $v(y, t)$ at the outlet were then computed by running a CFD simulation on this training block using our in-house CFD code, where u and v are

the horizontal and vertical components of the flow velocity, respectively. y is the vertical coordinate and t is the time. The pressure drop Δp between the inlet and outlet of a training domain was also collected from the dataset to further investigate the accuracy of the predicted pressure drop. Along with the flow and pressure drop data, the temperature distribution of $T(y, t)$, also computed by our in-house CFD, was trained to test the feasibility of predicting the heat transfer performance of a heat exchanger. However, it should be noted that any physical quantity, except temperature, can be trained using the current FLBB for additional applications if it is advected with the fluid flow. In this regard, the scope of use of the present work should not be limited to heat exchanger applications. For example, if the particle distributions are trained, the current procedure can be used to predict the particle capture performance for filtering applications.

After obtaining the u, v, Δp, and T outlet data from two different types of training blocks, with and without a cylinder in the first layer, these data were recursively used as inlet data in the second layer of the data generation process. Therefore, four different cases ($= 2^2$) were trained using the second data generation process. Following this training process, 2^n cases can be trained in the nth layer. In this study, the maximum training data was set to the eighth layer ($2^8 = 256$ cases). The total number of cases can be obtained up to the N-th layer

as $\sum_{n=1}^{N} 2^n$. Considering the dissipative nature of the fluid flow, which regulates the flow pattern after several layers, the prediction accuracy can sufficiently converge with a limited number of layers. In this study, we demonstrated the prediction performance of up to eight layers. The main benefit of using the present data generation process is that, as n increases, all possible flow patterns in heterogeneous cylinder arrays can be covered automatically and systematically. The data generation process does not require setting up a wide range of geometric configurations in the computational domain, which is a practical aspect of the proposed procedure.

It should also be noted that the data generated in the current procedure were free of the effects of artificial data selection on a specific flow pattern, and the ML methods are inherently dependent on data quality (Buda et al., 2018; Estabrooks et al., 2004; He & Garcia, 2009). Therefore, if the data selection is biased, it is difficult for the ML methods to make bias-free decisions (Buda et al., 2018; Estabrooks et al., 2004; He & Garcia, 2009). In our FLBB, a large number of downstream sets were systematically configured with recursive training using a given upstream block geometry. Thus, the amount of training data accumulated in the downstream direction will naturally cause a data imbalance. To address the data imbalance, resampling techniques, such as oversampling (adding minor data to the original dataset) or undersampling (removing the majority class from the original dataset), have been previously used (Buda et al., 2018; Estabrooks et al., 2004; He & Garcia, 2009). To avoid data imbalance, we employed the oversampling technique by duplicating the upstream block data to match the maximum amount of training data.

2.2. High-order flow-learned building block

In the previous section, we introduced the basic concept of the FLBB, which was inspired by the numerical discretization method. For conventional numerical techniques, a wide range of numerical schemes can be adopted to increase the prediction performance by adapting the flow characteristics or increasing the discretization accuracy (Ferziger & Peric, 2002). For example, the spatial derivative of the advective term in the Navier-Stokes equation can be resolved by adapting an upwind scheme that includes the flow characteristics of advection from upstream to downstream. Furthermore, a high-order upwind scheme using more spatial data points can be utilised to improve the numerical accuracy. In this regard, we suggested a high-order FLBB that considered flow characteristics.

In flows over cylinder arrays, dynamic flow effects, such as vortices, can vary depending on the gap distance between neighbouring cylinders (Sumner, 2010), which indicates spatial interdependency with the downstream object. Thus, the current one-way method of simply accumulating prediction results along the downstream direction may be insufficient for predicting the whole flow pattern due to a lack of downstream information. Here, we proposed a high-order approach that instructed building blocks to learn and prepare for possible downstream scenarios. As shown in Figure 1(d), there are four ways to combine the building blocks if the subsequent block is included as a dummy block to consider the downstream effects. In Figure 1(d), the subsequent dummy block is represented by a block surrounded by black dotted lines. Subsequently, by placing a cylinder in the subsequent dummy block, the learning process was extended to prepare all four scenarios.

This utilisation of a subsequent dummy block was analogous to the high-order scheme used to solve partial differential equations in conventional numerical analysis because it computes spatial derivatives using more data points to improve accuracy. Although more subsequent dummy blocks can be implemented to improve the prediction accuracy, we only considered one subsequent block, which we called the second-order FLBB approach.

2.3. Numerical formulation

In this study, data ware generated through two-dimensional numerical simulations using in-house code. The two-dimensional fluid flow and heat transfer over cylinder arrays was assumed to be incompressible and single-phase. The governing equations include mass, momentum, and energy conservation, defined as follows:

$$\nabla \cdot \mathbf{u} = 0, \tag{1}$$

$$\rho \left(\frac{\partial \mathbf{u}}{\partial t} + \mathbf{u} \cdot \nabla \mathbf{u} \right) = -\nabla p + \mu \nabla^2 \mathbf{u}, \tag{2}$$

$$\rho c \left(\frac{\partial T}{\partial t} + \mathbf{u} \cdot \nabla T \right) = k \nabla^2 T, \tag{3}$$

where $\mathbf{u}$ is the fluid velocity, ρ is the fluid density, p is the pressure, μ is the dynamic viscosity, T is the temperature, c is the specific heat capacity and k is the fluid conductivity. Here, the gravitational force was neglected and the working fluid properties (air, Pr = 0.71) were assumed constant to simplify the problem. The assumption of neglecting the change in fluid properties can be valid for cases with a sufficiently small temperature difference (Hasan, 2014; Herwig & Mahulikar, 2006; Rastan et al., 2021; Zargartalebi et al., 2020; Zargartalebi & Azaiez, 2019). For example, for our targeted problem of Re = 100

and a cylinder diameter of 100 μm, a temperature difference of 20 K would fall within an acceptable range for considering constant property fields (Herwig & Mahulikar, 2006). Thus, the temperature difference between the inlet and the cylinder wall has been set to 20 K. The change in the fluid property field with larger temperature difference will be included in the future work to reflect more realistic heat transfer characteristic.

The governing equations were integrated using Chorin's projection method (Chorin, 1968), and then the discrete form of the equation could be written as follows:

$$\frac{\mathbf{u}^{n+1} - \mathbf{u}^n}{\Delta t} = \frac{1}{\rho}\mathbf{A}^n - \frac{1}{\rho}\nabla p, \qquad (4)$$

where the advection and diffusion terms are represented by $\mathbf{A}$. The momentum equation could be split into two parts as:

$$\frac{\tilde{\mathbf{u}} - \mathbf{u}^n}{\Delta t} = \frac{1}{\rho}\mathbf{A}^n, \qquad (5)$$

$$\frac{\mathbf{u}^{n+1} - \tilde{\mathbf{u}}}{\Delta t} = -\frac{1}{\rho}\nabla p, \qquad (6)$$

where we introduced the variable $\tilde{\mathbf{u}}$, which is the new fluid velocity when the effect of pressure is ignored. The first step is to obtain this velocity using Equation (5). The pressure is then obtained by taking the divergence of Equation (6) and enforcing to be divergence free. This led to a Poisson equation for the pressure:

$$\nabla \cdot \left(\frac{1}{\rho}\nabla p\right) = \frac{\nabla \cdot \tilde{\mathbf{u}}}{\Delta t}. \qquad (7)$$

The Poisson equation was solved fast by FISHPACK (Adams et al., 2016) software library. Finally, the updated velocity field is computed as

$$\mathbf{u}^{n+1} = \tilde{\mathbf{u}} - \frac{\Delta t}{\rho}\nabla p. \qquad (8)$$

The first order forward Euler integration was employed for the temporal discretization, and the Eulerian finite difference method on staggered grids (Harlow & Welch, 1965) was employed for spatial discretization of velocity and pressure. The convective term was computed using a second-order ENO procedure (Shu & Osher, 1988). To implement cylindrical solid objects, the Ghost Fluid Method (GFM) (Tseng & Ferziger, 2003) was used. The computational nodes were classified into nodes of fluid or solid. Each node was identified with the distance function field from the nearest solid. The flow field was solved with the boundary condition specified at ghost nodes. The values at ghost nodes were extrapolated to satisfy the intended boundary condition at the solid object which

is zero for the current study. Please see more detailed information of GFM procedure in the literature (Tseng & Ferziger, 2003).

The developed numerical method has been verified with two benchmark tests of flow over a single cylinder ($Re = 40$), and flow over in-line two tandem cylinders ($Re = 100$) in the two-dimensional geometry. The benchmark tests were carried out for Reynolds up to 100 considering the target range of the current study. Outside this range, the flow may not be two-dimensional since the first 3D instability might occur at $Re = 189$ (mode A) and the second instability at around $Re = 259$ (mode B) (Barkley & Henderson, 1996).

Firstly, we performed grid convergence tests for uniform flow over a single cylinder which has large amount of reference data to be compared. The computational domain size was $32D \times 16D$ where D represents the diameter of the cylinder. For boundary conditions, free stream boundary conditions ($u = U_{in}$, $v = 0$) and Neumann pressure condition were applied at the inlet (left side in this test), top, and bottom sides. Outflow condition, i.e. zero normal gradient for velocity and zero pressure, was applied at the outlet (right side in this test), and noslip wall at the surface of circular cylinder, which was positioned $8D$ from the inlet. Each pressure coefficient $C_p = F_p/(0.5\rho U_{in}^2)$, and skin-friction coefficient $C_f = F_\tau/(0.5\rho U_{in}^2)$ along the cylinder surface (with respect to angular α) at $Re = 40$ was measured with CPD (cells per diameter), and compared with the reference data (Tseng & Ferziger, 2003) as shown in Figure 2(a). Here, the F_p and F_τ represent the pressure drag normal to and skin-friction drag parallel to the surface of the cylinder, respectively. These components contribute to the total drag force acting on a cylinder. At higher Re number, pressure drag due to vortex shedding can be larger than that caused by the skin friction drag (Baranyi & Lewis, 2006). Figure 2(a) shows that the numerical results denoted by the red circle, blue triangle, and green diamond were converged with the increasing number of grids (represented by CPD) for each C_p (left) and C_f (right), and converged results were close to the reference data denoted by the black solid line. Based on these results, we employed the grid resolution of CPD=32, corresponding to 64×64 in the training domain.

In addition to the flow over a single cylinder, the flow over in-line tandem two cylinders was simulated to verify the accuracy of the flow over multiple solid bodies involving complex interactions between the wakes, and vortex streets. The computational domain was $40D \times 20D$ with the same boundary conditions as Figure 2(a) (flow over a single cylinder). The time-averaged C_p of the upstream cylinder, denoted by P1 (left) and downstream cylinder, denoted by P2 (right) were measured at $Re = 100$
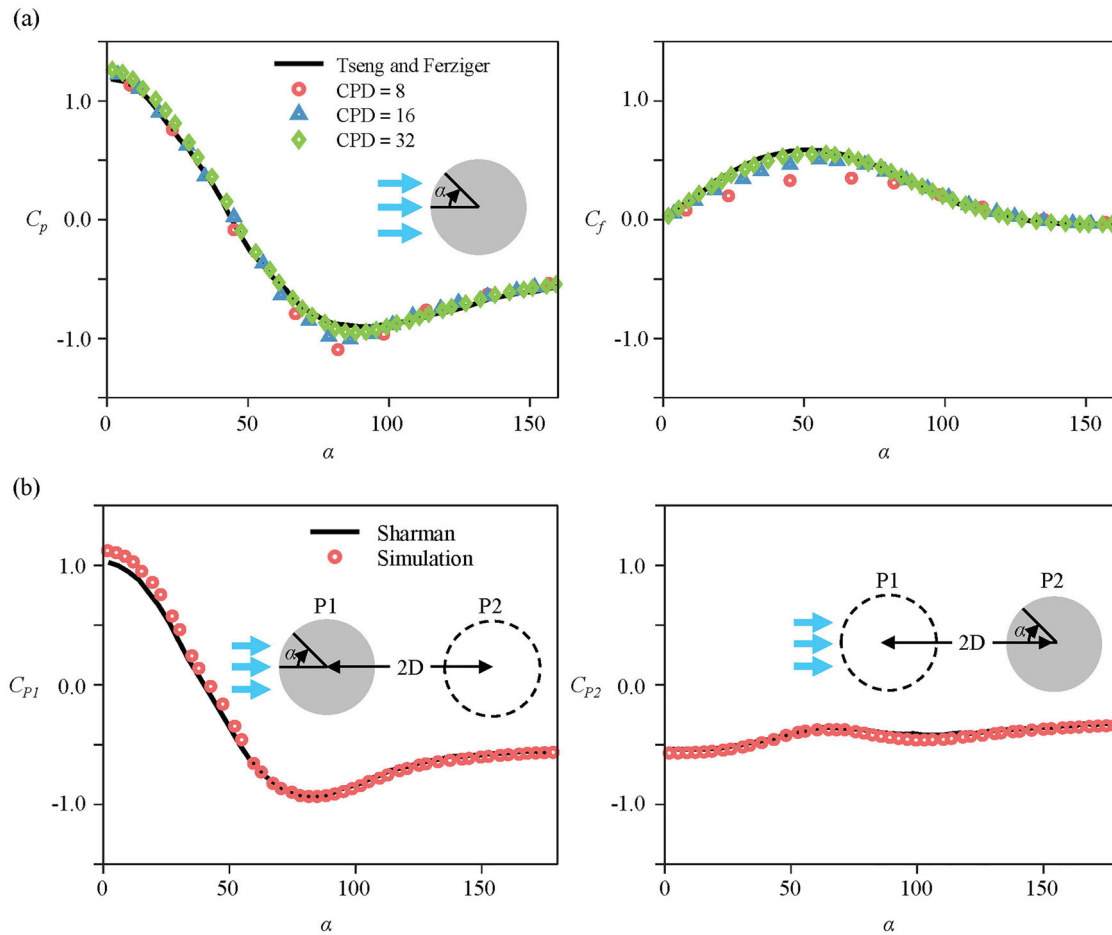
Figure 2. Benchmark tests for the code validation. (a) Grid resolution tests for flow over a single cylinder. (b) Measurement of pressure coefficient C_{P1} (left) and C_{P2} (right) in flow over in-line tandem cylinders.

as shown in Figure 2(b), and compared with the reference data (Sharman et al., 2005) denoted by the black solid line. The results for each C_{P1} and C_{P2} were in good agreement with the reference data.

2.4. Simulation setup

The computational domain for data generation in the first-order FLBB is depicted in Figure 3(a) and has dimensions of $16D \times 2D$. Periodic boundary conditions were applied to the top and bottom side. At the inlet, boundary conditions of specific values of $u(y,t)$, $v(y,t)$, and $T(y,t)$ were imposed. A zero normal gradient for velocity and zero pressure were applied at the outlet, while a no-slip wall condition and a constant wall temperature (20 K higher than the inlet bulk temperature) were imposed on the surface of the circular cylinder. Here, y is the vertical position at the inlet and t is time. The grid resolution in the training domain, marked by the red dashed box in Figure 3(a), was 64×64 (CPD = 32). The training domain represents the corresponding building block with or without a cylinder. To prevent the blockage

effect, the longitudinal length L_c was set to $8D$, ensuring the uniform velocity without disturbance by the presence of cylinder. For correlating the inlet and outlet flow data in subsequent simulations, L_c was set to D. For the second-order FLBB, the extended cases of computational domains were employed to address the geometric configuration in the subsequent dummy domain as depicted in Figure 3(b). The target flow's computational domain has dimensions of $32D \times 2D$ as depicted in Figure 3(c). The target domain consists of ten subblocks aligned along the flow direction.

2.5. Neural network-based regression model

In this section, we introduce the NN architecture to correlate flow data in each inlet and outlet face of the block. As mentioned previously, state-of-the-art ML techniques have been developed and implemented successfully for various engineering problems (Brunton et al., 2020; Duraisamy et al., 2019). Here, we focused on the development of a basic concept and implementation of the FLBB with a systematic data generation process; thus,
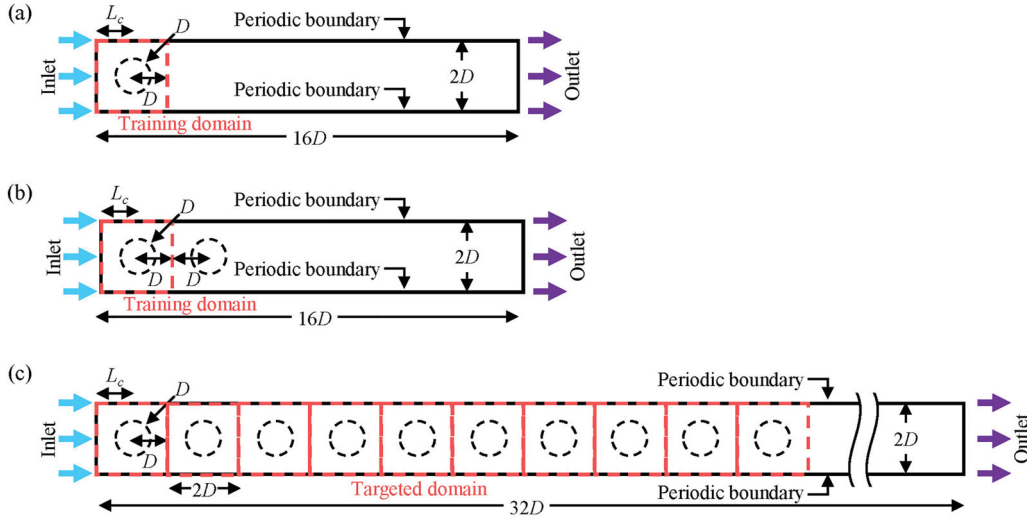
Figure 3. Simulation setup. (a) The computational domain for data generation of the first-order approach. (b) The computational domain for data generation of the second-order. (c) The computational domain for target flow domains.

a well-known basic structure of the NN was utilised to describe the correlation between the inlet and outlet data.

NNs are well-known universal function approximators (Hornik et al., 1989; Jin et al., 2021; Raissi et al., 2019) that do not infer the correlations between the input and output variables. We herein took advantage of NN's aforementioned capability to predict flow variables at the outlet (right side face in this study), we used the NN to predict flow variables at the outlet (right-side face of a subblock) with given flow variables at the inlet face. The correlations between the inlet and outlet flow data for two (first-order FLBB) or four (second-order FLBB) building blocks, depending on the geometric configuration, were independently learned using different NNs; thus, we had two or four distinctive function approximators. NNs with three hidden layers of 193 nodes were employed, and the rectified linear unit (ReLu) activation function (Krizhevsky et al., 2012) was implemented in each layer, except the final layer, to ensure that the output values were unbounded. While the NNs were trained using datasets, the weight parameters were updated to minimise the following mean squared error (MSE):

$$\text{MSE} = \frac{1}{N} \sum_{i=1}^{N} (Y_i - \widetilde{Y}_i)^2, \qquad (9)$$

where Y_i and $\widetilde{Y}_i$ denote the target data retrieved from the numerical simulations and the results predicted by the NNs, respectively, and N represents the number of data points. Initially, the weight parameters were randomly generated according to a normal distribution. To update the weight parameters, we used the Adam optimiser

(Kingma & Ba, 2014) with a learning rate of 10^{-3} for 1000 training epochs. The open-source software, Keras (Chollet, 2018), was used for training the NN-based regression model. The NN training took less than 1 min based on eight data layers, and predicting the target flow domain (10 blocks) using the trained NNs took 1 s (Intel Xeon Gold 6230 CPU 2.10 GHz, 187GB memory). The simulation for data production took approximately 40 min per case, and the direct computation of the target geometry took approximately 1.5 h. Because our main objective was to develop a systematic data-generation procedure, further optimisation is beyond the scope of this study and will be considered in the future with additional geometries (i.e. staggered) or input conditions.

The training data for u, v, Δp, and T were normalised to $u^* = u/U_{\max}$, $v^* = v/U_{\max}$, $\theta = (T - T_{in})/(T_w - T_{in})$, and $\Delta p^* = \Delta p/(\rho U_{\max}^2)$. Here, $U_{\max} = U_{in}S_T/(S_T - D)$ represents the maximum velocity through the cylinder arrays, which is typically used in conventional heat exchanger analyses (Incropera et al., 1996), where D is the diameter of the cylinder and S_T is the transverse distance between the cylinders, as shown in Figure 1(a). T_{in} and T_w represent the bulk temperature at the inlet of the target block and wall temperature of the cylinder, respectively. The magnitude of the bulk temperature increased across the cylinders (acting as heat sources); thus, the difference between the bulk and object temperatures (i.e. the driving potential for energy transfer) decreased. Therefore, scaling the temperature with a uniform inlet temperature of the first layer may be inappropriate when the energy potential, that is, the difference between the bulk and object temperatures, decreases. To address this localised energy potential more adequately,

we rescaled the temperature to the bulk inlet temperature of each learning block. The normalised quantities guaranteed that the training data were of the order of one. The normalised pressure drop was scaled by the kinetic energy and drag coefficient because the pressure loss was not proportional to the kinetic energy alone. By scaling the kinetic energy and drag coefficient, the normalised pressure drop remained near unity regardless of the Reynolds number. The Reynolds number Re and scaled inlet flow variables $u*$, $v*$, and θ along the 64 vertical nodes in the computational domain were utilised as inputs for the NNs. The scaled outlet flow variables $u*$, $v*$, and θ with normalised pressure drop $\Delta p*$ were utilised as outputs for the NNs. The prediction accuracy was evaluated using L_2 and L_∞ defined as follows (Lee & You, 2019):

$$L_2 = \left(\frac{1}{4} \left[\frac{1}{n} \sum_i^n \{ (u_i^* - \widetilde{u}_i)^2 + (v_i^* - \widetilde{v}_i)^2 \right. \right.$$
$$\left. \left. + (\theta_i - \widetilde{\theta}_i)^2 \} + (\Delta p^* - \Delta \widetilde{p})^2 \right] \right)^{\frac{1}{2}}, \quad (10)$$

$$L_\infty = \frac{1}{4} \left(\max_i |u_i^* - \widetilde{u}_i| + \max_i |v_i^* - \widetilde{v}_i| \right.$$
$$\left. + \max_i |\theta_i - \widetilde{\theta}_i| + |\Delta p^* - \Delta \widetilde{p}| \right), \quad (11)$$

where $\tilde{u}$, $\tilde{v}$, $\tilde{\theta}$, and $\Delta \tilde{p}$ are normalised data predicted by the NNs. n denotes the number of grids in the transverse direction. In addition to the L_2 evaluation, as in Equation (11), in each subblock, the arithmetic mean of L_2 over the entire block was also measured to present the overall prediction performance of the entire array more intuitively.

3. Results

3.1. First order approach vs. second order approach

To verify the flow prediction capability of the building block that learned the systematic flow data, we tested many heterogeneous combinations of cylinder arrays, and we present a few representative examples in this paper. By solving these examples, the prediction accuracy and robustness of the FLBB were examined with respect to the number of layers in the training dataset. Figure 4 shows that the spatial domain is discretized into ten subblocks and the six circular cylinders are randomly distributed in this array with different pitch distances between neighbouring cylinders. Prediction tests were then performed for different flow regimes with three different Reynolds numbers ($Re = \rho U_{in} D / \mu$) of 1, 10, and 100, where ρ is the fluid density, U_{in} is the fluid velocity at the inlet, and μ is the fluid viscosity. The Reynolds numbers were selected to cover the various flow behaviours in terms of vortex formation (Munson et al., 2013). For small Reynolds numbers ≤ 1, the fluid flow through a cylinder array was fully laminar with little vortex behaviour in the wake of a cylinder. When Re increased to the order of ten, a vortex appeared in the wake of the cylinder; however, there was no shedding. If Re increased further above 100, the vortex separated from the cylinder and began to shed downstream. To test the prediction capability of the heat transfer performance, a fluid was introduced with an initial temperature of T_{in} uniformly distributed along the inlet. The walls of the cylinders were set to maintain constant temperature T_w.

In this section, we use the representative geometric case of a randomly arranged cylindrical array, as shown in Figure 4(a), and we explain in detail how the proposed FLBB predicts time-averaged flow data that vary according to different local cylinder arrangements and
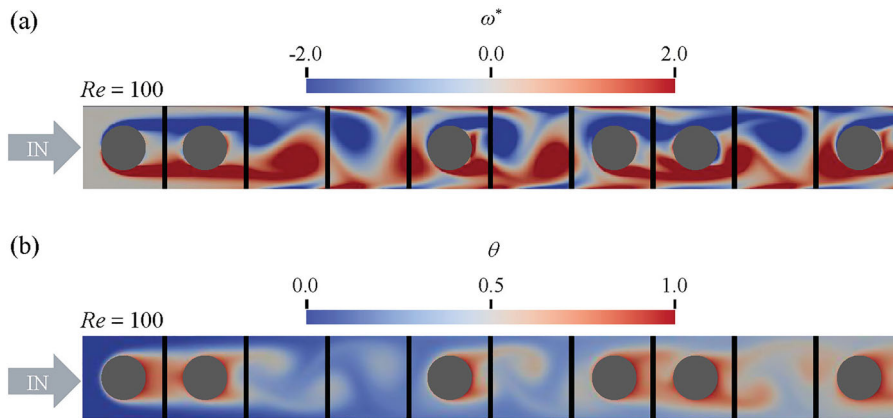

Figure 4. (a) Instantaneous normalised vorticity $\omega*$ contour and (b) normalised temperature θ contour at $Re = 100$. The output data of the flow and temperature profiles were obtained at the outlet of each subblock denoted by thick black solid lines.

Reynolds numbers. In addition to the representative case, other random structures were tested to verify the prediction performance of the proposed approach, as described in the following section. Figures 5–7 show the prediction results for the representative geometric case with a Reynolds number of 100, which is more difficult for flow prediction than the other Re cases of 1 and 10 because the vortices remain shedding in the wake of a cylindrical cylinder and co-shedding can also occur depending

on the pitch spacing between neighbouring cylinders at $Re = 100$ (Sumner, 2010). Figure 4(a) displays a colour map of the instantaneous normalised vorticity of $\omega^* = D/U_{in}(\partial v/\partial x - \partial u/\partial y)$, which presents a tortuous pattern, indicating that the vortices continue to shed in the wake of a cylinder. The red colour in the colour map of the normalised vorticity denotes counterclockwise vorticity, whereas the blue colour denotes clockwise vorticity. In addition, a colour map of the instantaneous
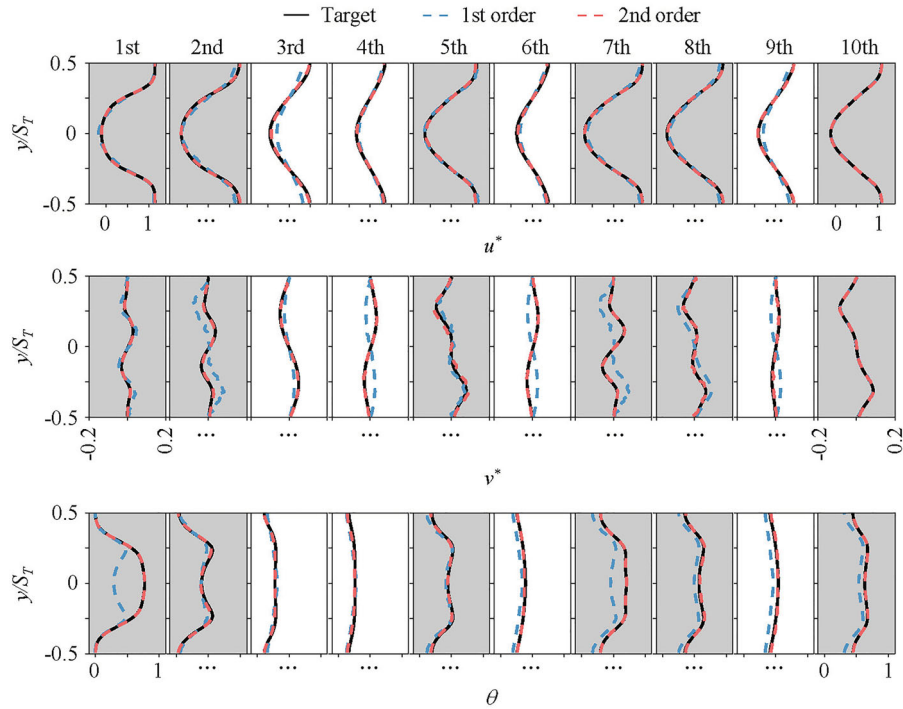

Figure 5. Predictions for vortex shedding flow ($Re = 100$) and temperature distributions over an in-line cylinder array with random pitch distances. Predicted data of $u*$, $v*$, and θ by the first-order approach (blue) and second-order approach (red) are compared to the target data (black). In the plots, the white and grey backgrounds represent void and filled subblocks, respectively.
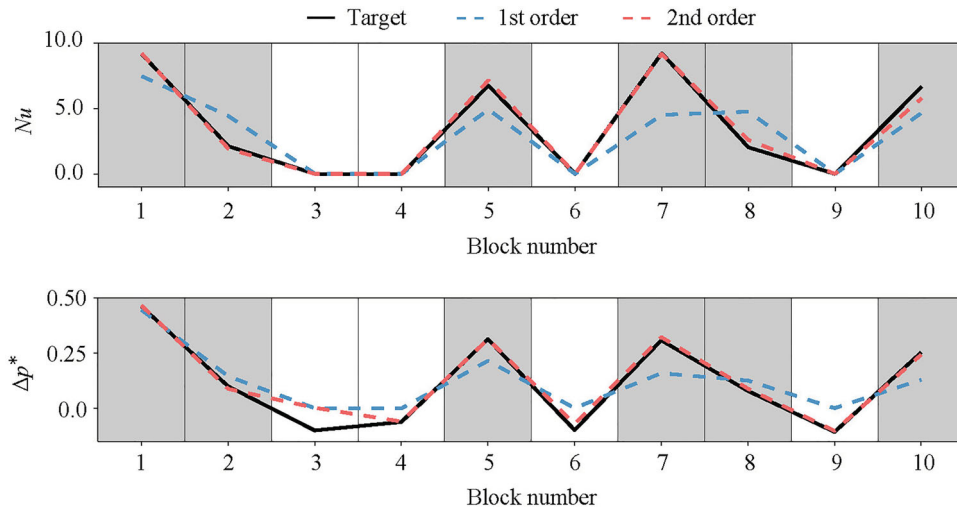

Figure 6. Predicted data of Nu (first row) and Δp^* (second row) by the first-order approach (blue) and second-order approach (red) are compared to the target data (black) at $Re = 100$.

normalised temperature of the θ-distribution is shown in Figure 4(b). Owing to the time-varying cyclic nature of vortex shedding, $u*$, $v*$, θ, and Δp^* vary cyclically over time. This cyclic nature is a unique flow characteristic of the vortex-shedding flow in comparison to a static flow without vortex shedding at $Re = 1$ and 10, which will be discussed later with the cases in Figures 8–11. The output data of the flow and temperature profiles were obtained at

the outlet of each subblock denoted by thick black solid lines.

Here, we compare the predicted results to each first- and second-order approach to the target data, and discussed which approach can describe the flow characteristics more properly. A localised comparison of the outlet profiles of each building block is shown in Figure 5. The predicted velocity and temperature profiles were
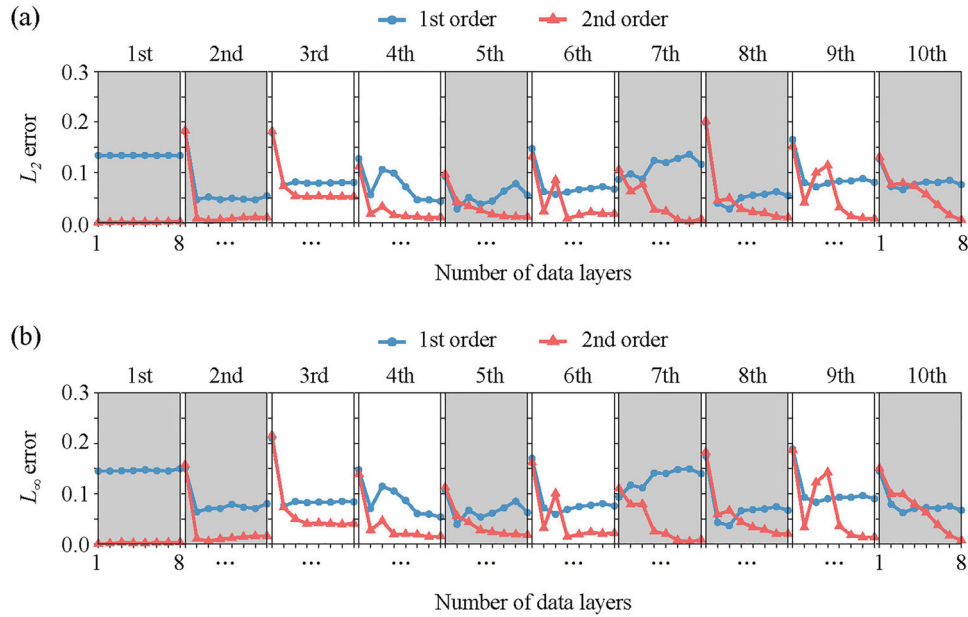

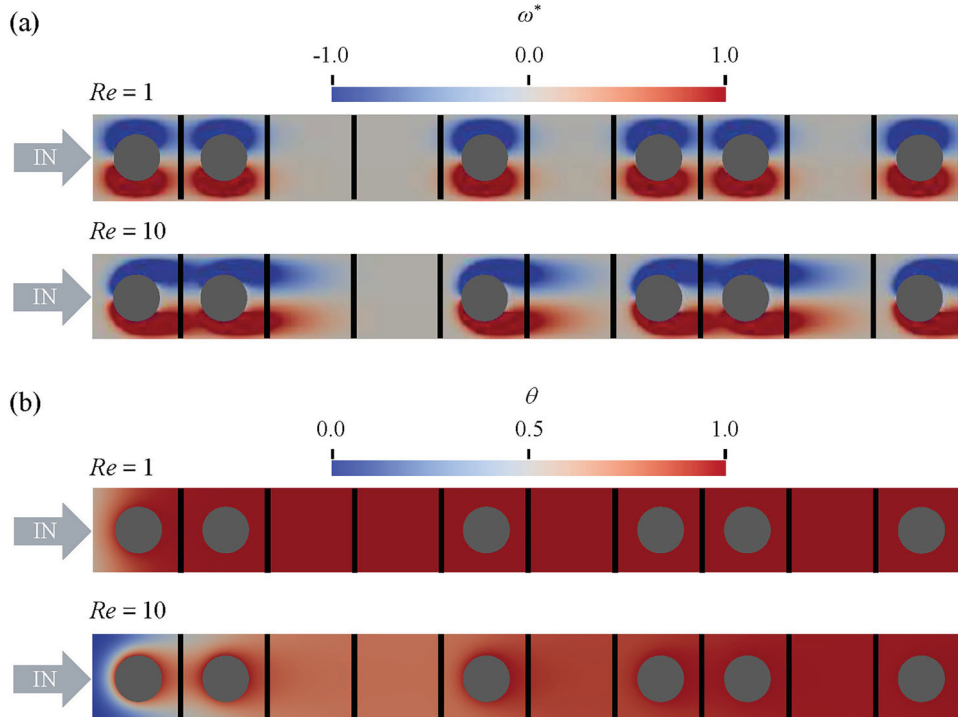**Figure 7.** Prediction errors versus the number of data layers: (a) the L_2 and (b) L_∞ errors.

Figure 8. (a) Instantaneous normalised vorticity $\omega*$ contour and (b) normalised temperature θ contour at $Re = 1$ and $Re = 10$.
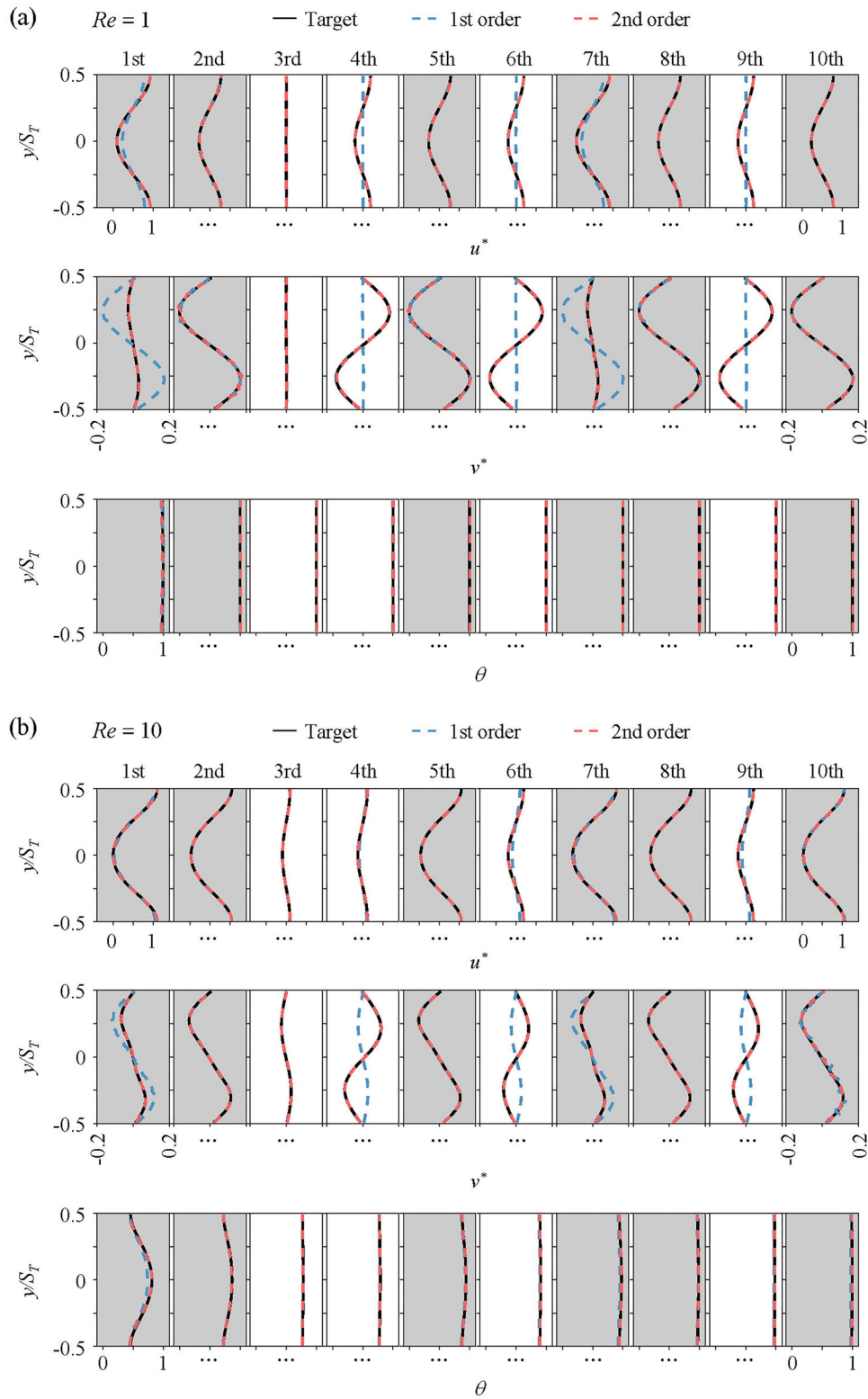
Figure 9. Predicted data of u_*, v_*, and θ by the first-order approach (blue) and second-order approach (red) are compared to the target data (black) at (a) $Re = 1$ and (b) $Re = 10$.

compared to the target profiles. All predicted values were generated using the largest dataset of eight layers to obtain the highest accuracy. The graphs in the first rows

of Figure 5 plots the time-averaged and normalised horizontal flow velocities of u_* (x axis) along the vertical coordinate of y/S_T for every block. The graphs show
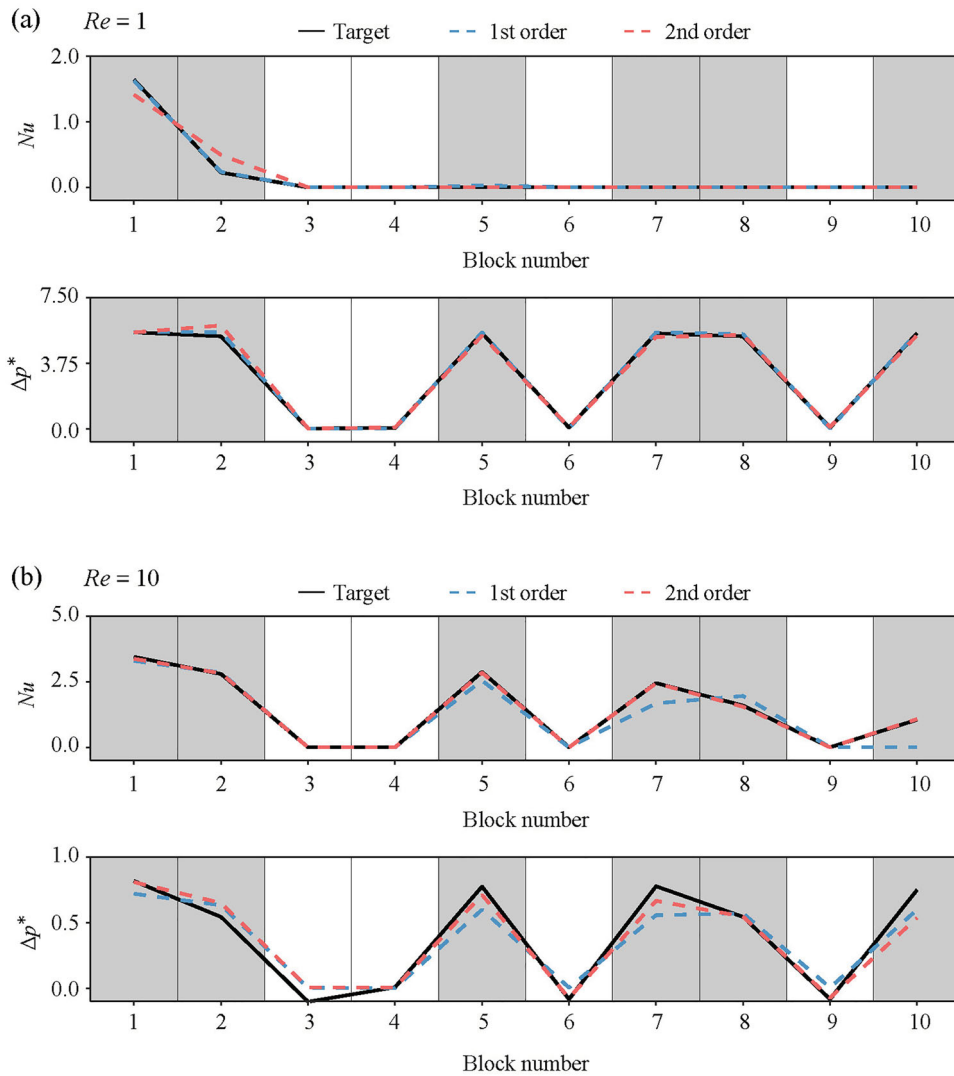
Figure 10. Predicted data of *Nu* and Δp^* using the first-order approach (blue) and second-order approach (red) are compared to the target data (black) at (a) *Re* = 1 and (b) *Re* = 10.

that the second-order approach (red dashed curves) provided surprisingly accurate predictions for all the blocks when compared to the target data (black curves). The first-order approach (blue dashed curves) also shows reasonable predictive accuracy with regard to the $u*$ prediction. For the time-averaged and normalised vertical flow velocities of $v*$, serious prediction errors of the first-order approach were observed in the 4th, 6th, and 9th blocks. These errors were particularly serious because the first-order approach failed to predict not only the flow magnitude but also the flow direction. The plots shown in the second row of Figure 5 show the inverted flow profiles between the first-order predictions and the target data in the 4th, 6th, and 9th blocks. This contrasts with the $u*$ prediction, for which the first-order approach was able to describe flow profiles similar to those of

the target profiles; the first-order approach failed to predict an accurate flow magnitude. Interestingly, the 4th, 6th, and 9th blocks, all of which had severe $v*$ prediction errors, shared the same geometric configuration as the void block, without a cylindrical object connected to the subsequent block with a cylinder in the downstream direction. This is because a flow profile with vortex shedding is subjected to reversal when it passes close to a cylinder (Meneghini et al., 2001). In other words, the first-order approach failed to describe flow reversal near a cylinder, that is, strong interdependency between objects. Conversely, the second-order approach was able to accurately describe flow reversal near a cylinder.

Compared to the velocities, the first-order approach produced more noticeable errors for the normalised temperature prediction of θ. The graphs in the third row of
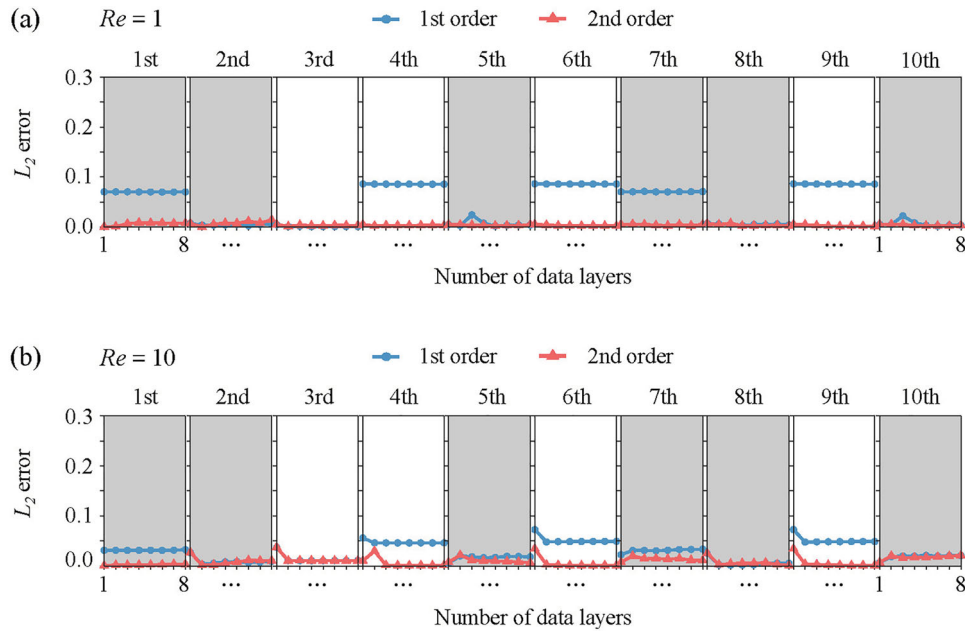
(a) $Re = 1$

(b) $Re = 10$

Figure 11. The L_2 errors are plotted versus the number of data layers at (a) $Re = 1$ and (b) $Re = 10$.

Figure 5 show that the first-order approach fails to predict both the temperature profile and magnitude in almost all blocks. The poor prediction performance, particularly for temperature, was attributed to the increased interdependency of the neighbouring building blocks in the heat equation. To describe the temperature distribution, the Navier-Stokes equations should be solved simultaneously with the heat equation, which also has strong interdependency, partly owing to the elliptic nature of heat diffusion (Meneghini et al., 2001). Consequently, the first-order approach, which was incapable of addressing spatial interdependency, had poor temperature prediction capabilities. The elliptic nature of the heat equation reflects the heat transfer characteristics during conduction. Conductive heat transfer occurs from a higher to a lower temperature, which means that it can propagate even along the direction opposite to the fluid flow. The surfaces of the cylindrical objects shown in Figure 4(b) have a higher temperature than the fluid passing around it because this array is designed to model the most common engineering problem of cooling down the fluid flowing inside the cylindrical objects (Bhuiyan & Islam, 2016; Faghri & Zhang, 2006; Gorman et al., 2019; Lee et al., 2013). In this regard, heat was assumed to be transferred from a hotter cylinder wall to a colder fluid. Notably, among all temperature predictions by the first-order approach, those in the 1st and 7th blocks showed extremely poor performance. This is due to the locally slow behaviour of the flow between the cylinders when the two cylinders were close to each other. As a result, the conduction effect of the heat source (cylinder) inside

the subsequent block became significant, and the prediction results from the first-order approach, which does not consider this spatial interdependency, worsened considerably. Accordingly, the predicted heat transfer rate Q driven by the predicted temperature was poor when using the first-order approach. In contrast, the second-order approach was found to predict the temperature distribution significantly well, demonstrating its superior ability to address spatial interdependency, including conductive heat transfer.

We also present the Nusselt number $Nu = QD/(kA \Delta T_{LMTD})$ derived from the predicted temperature profiles and normalised pressure drop Δp^* along the flow direction in Figure 6, where Q denotes the heat transfer rate of $Q = \dot{m}C_p(T_{out} - T_{in})$ along the flow direction, A denotes the surface area of the cylinder, k denotes the thermal conductivity of the fluid, and ΔT_{LMTD} denotes the log mean temperature difference. Figure 6 compares the predicted and target data for Nu and Δp^* at the inlet and outlet of each block versus the block order. The results show a very accurate heat transfer across the randomly distributed cylinders, which is impossible to obtain from the conventional heat transfer correlation. Both the first- and second-order approaches provided reasonably accurate predictions of the pressure drop. This is because the pressure drop is primarily determined by the drag from a cylindrical object, which is heavily dependent on the velocity profile; therefore, the type of block (void or filled) has a greater influence on prediction accuracy than the spatial interdependency with nearby blocks. However, the second-order approach

(red-dotted curve) provided a relatively more accurate prediction, demonstrating its superiority over the first-order approach.

The prediction performance of the FLBB was further evaluated by calculating the L_2 error for each subblock with respect to the number of layers of training data from one to eight, as shown in Figure 7. Here, L_2 estimates the prediction error, which is calculated by comparing the predicted quantities $u*$, $v*$, θ, and Δp^* by ML to the target values obtained by computing the entire simulation domain in Figure 7(a). The plots in Figure 7(a) show that the prediction error L_2 generally decreases or converges with an increasing number of training layers because the prediction errors decrease as the amount of training data increases. As shown in Figure 7(a), there is a significant difference in the predictive performance between the first- and second-order approaches. Figure 7(a) shows that for the first-order approach, the L_2 error for the 1st block exceeds 0.1, and from the 3rd block onward, the error gradually increases, implying that the prediction error accumulates along the flow direction. The error accumulation was not relieved, even with an increase in the training data up to eight layers. Conversely, the second-order approach shows that, except for the 6th and 9th blocks, the L_2 error can be significantly reduced with only two or more layers. One distinct advantage of the second-order approach is that the L_2 errors can be successfully reduced using five or more layers, including the 6th and 9th blocks. This is because the second-order approach, which was designed to prepare for all possible scenarios in advance, functions only when a certain level of data is collected. A more positive aspect of the second-order approach is that, unlike the first-order approach, the L_2 error always decreases as the number of data layers increases, which demonstrates the high robustness of the present FLBB in terms of prediction capability. As a result, all blocks achieved the highest level of prediction accuracy ($L_2 < 0.05$) for the eight layers of training data. Notably, five layers were acceptable for training, considering that most of the errors were below 0.1, which was treated as a fair criterion (Lee & You, 2019; Raissi et al., 2020). Fewer layers were sufficient for lower Reynolds numbers (see Figure 11). In addition to L_2, L_∞ error was measured to quantify the prediction error caused by the outlier data generated by the current FLBB. The plots shown in the second row of Figure 7(b) presents similar L_∞ values to the L_2 values in the first row for all blocks for both the first- and second-order approaches. This implies that both approaches are stable because they do not create outliers.

The high prediction performance of the second-order approach was extended to cases with Reynolds numbers of 1 and 10 (Figure 8), where the vortex was not shed.

As previously stated, the colour map in the first row of Figure 8(a) shows that the vorticity is weakly formed in the wake of the cylinder at $Re = 1$. Weak vorticities were only observed near the cylinder because the fluid flow was assumed to rotate slightly when it passed through the cylinder. The instantaneous vorticity field ω in the first row of Figure 8(a) shows that the fluid flow is not tortuous, as shown in Figure 4(a) for $Re = 100$. Figure 8(b) depicts the instantaneous normalised temperature contours for Reynolds numbers of 1 and 10. In contrast to the case of $Re = 100$, the convective impact of the cold fluid was very small.

Figure 9(a and b) present the predicted data of $u*$, $v*$, and θ of the first- and second-order approaches at Reynolds numbers of 1 and 10, respectively, compared to the target data. The results obtained using the second-order approach closely matched the target data for both Reynolds numbers. However, the predictions made by the first-order approach exhibited poor velocity prediction in some blocks. In the first row of Figure 9(a), the horizontal velocity predicted by the first-order approach in the 4th, 6th, and 9th blocks shows slight inaccuracies; however, overall, it demonstrates reasonable predictive performance. Conversely, the vertical velocity predictions of the first-order approach are very poor, as shown in the second row. In particular, the results for the 1st, 4th, 6th, 7th, and 9th blocks are particularly inaccurate because they share the geometric characteristic of being subsequent blocks filled with a cylinder. This trend was also observed at the Reynolds number of 10 (Figure 9(b)). The temperature predictions at Reynolds numbers of 1 and 10 were relatively accurate, with good agreement between the predicted and target data. In addition, we compared the predicted Nu and Δp^* using the first- and second-order approaches at $Re = 1$ and $Re = 10$, as shown in Figure 10(a and b). Our findings demonstrate that both approaches performed well in approximating the target data for Nu, which can be attributed to their accurate prediction of the temperature, as shown in Figure 9.

The plots in Figure 11(a and b) compare the L_2 errors for the first- and second-order approaches with the number of training data layers in each block at $Re = 1$ and $Re = 10$, respectively. Unlike the second-order approach, the first-order approach showed a large difference in the L_2 error between each block. To be more specific, the first-order approach presented good prediction performance for the 2nd, 3rd, 5th, 8th, and 10th blocks, whereas it had limited prediction capability for the 1st, 4th, 6th, 7th, and 9th blocks. This implies that there are combinations of cylindrical objects and flow conditions that the first-order approach cannot handle well. The high prediction errors by the first-order approach did not decrease

with an increasing number of training data layers up to eight. This is because the spatial inter-dependency is not determined simply by the dynamic flow effect. From a mathematical perspective, it is rather normal for the spatial interdependency to increase at lower Reynolds numbers because the elliptic nature of both the Navier-Stokes and heat equations is inversely proportional to the Reynolds number (Faghri & Zhang, 2006). Conversely, the second-order approach produced accurate predictions with a low $L_2 < 0.02$ for all blocks, as shown in Figure 11, indicating that the second-order approach can successfully address problems of a higher elliptic nature at lower Reynolds numbers. We can also see that the prediction accuracy for these low Reynolds number flows was practically acceptable (L_2 successfully converges to near-zero values) with three layers of training data.

To compare the prediction performance more intuitively, the arithmetic mean of L_2 was computed for all the building blocks. In Figure 12, the mean L_2 error is plotted against the number of data layers for three different Reynolds numbers (1, 10, and 100). The superiority of the second-order approach over the first-order approach can be observed more clearly for all three flow regimes. The most notable feature of the second-order approach was that the mean L_2 error consistently decreased as the number of training data layers increased for all three Reynolds numbers, whereas the mean L_2 error from the first-order approach remained large. This is an important feature for ensuring prediction robustness (IEEE Standards Board, 1990; Xu & Mannor, 2012; Zhang et al., 2019). At $Re = 1$, as shown in Figure 12, the mean L_2 error was observed to converge quite early from a small number of datasets (the 1st layer) for both the first- (blue) and second-order (red) approaches. This is because the flow patterns at a small Reynolds number of unity were described relatively easily, even with a few datasets, because the dynamic vortex-solid interaction was limited at this Reynolds number.
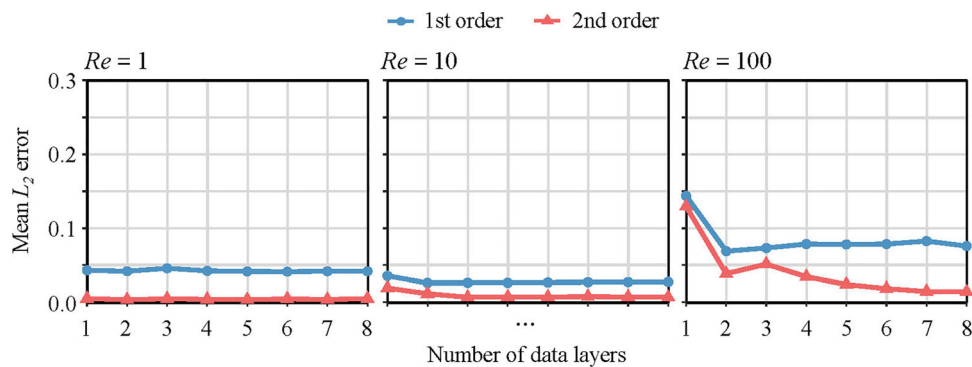

Figure 12. Mean L_2 errors by the first-order approach (blue) and second-order approach (red) are plotted versus the number of training data layers at three different Reynolds numbers of 1, 10, and 100.
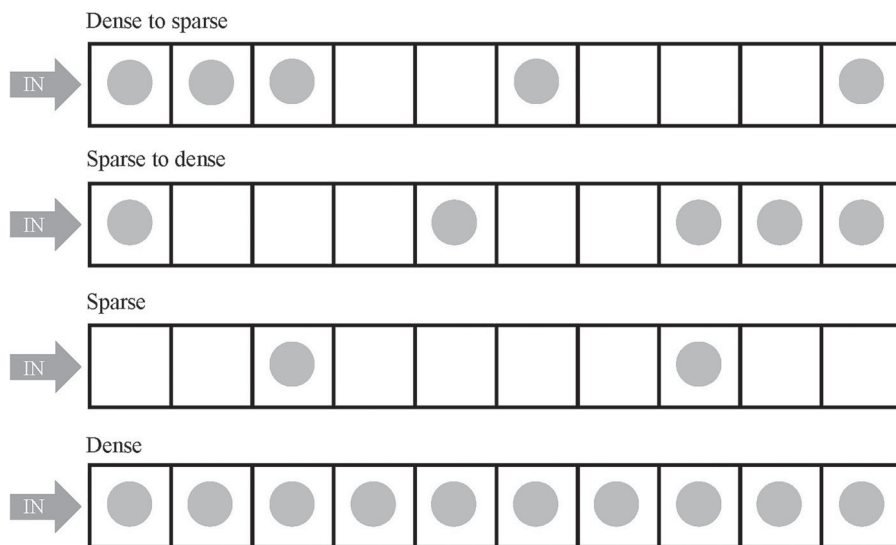

Figure 13. The four characteristic arrangements of 'dense to sparse', 'sparse to dense', 'sparse', and 'dense', which are representative of practical applications of engineering cylinder arrays, are employed to verify the robustness of the current FLBB approach.

As the Reynolds number further increased beyond 10–100, the mean L_2 error of the first-order approach increased.

3.2. Further characteristic geometries

In addition to the representative geometries presented in Figures 4 and 8, other random geometric configurations were investigated to test the prediction performance of the current FLBB. Some characteristic geometries investigated in this study are discussed in this section. Figure 13 shows four characteristic geometries: dense-to-sparse (first row), sparse-to-dense (second row), sparse (third row), and dense (last row). These four geometries are representative of actual applications of heat exchangers and particulate matter filters that have been used in practice (Khan et al., 2006; Li et al., 2016; Zargartalebi et al., 2020). The dense arrangement shown in the last row of Figure 13, which is the most basic homogeneous geometry among solid engineering arrays, was also included in this study. Because the present FLBB was designed to cover all possible geometric configurations, it should be applicable to heterogeneous arrays and homogeneous structures.

The predicted Nu, which is a major parameter in many engineering applications, using the second-order approach (in red) with eight data layers at $Re = 1$, $Re = 10$, and $Re = 100$, for these four characteristic geometries, was compared to the target data (in black) in Figures 14–16. For more localised flow data for $u*$, $v*$, θ, and $\Delta p*$, please refer to the Supplementary material. The results in Figures 14–16 indicate that the predicted Nu values are in close agreement with the target Nu values for the four characteristic geometries at $Re = 1$, 10,
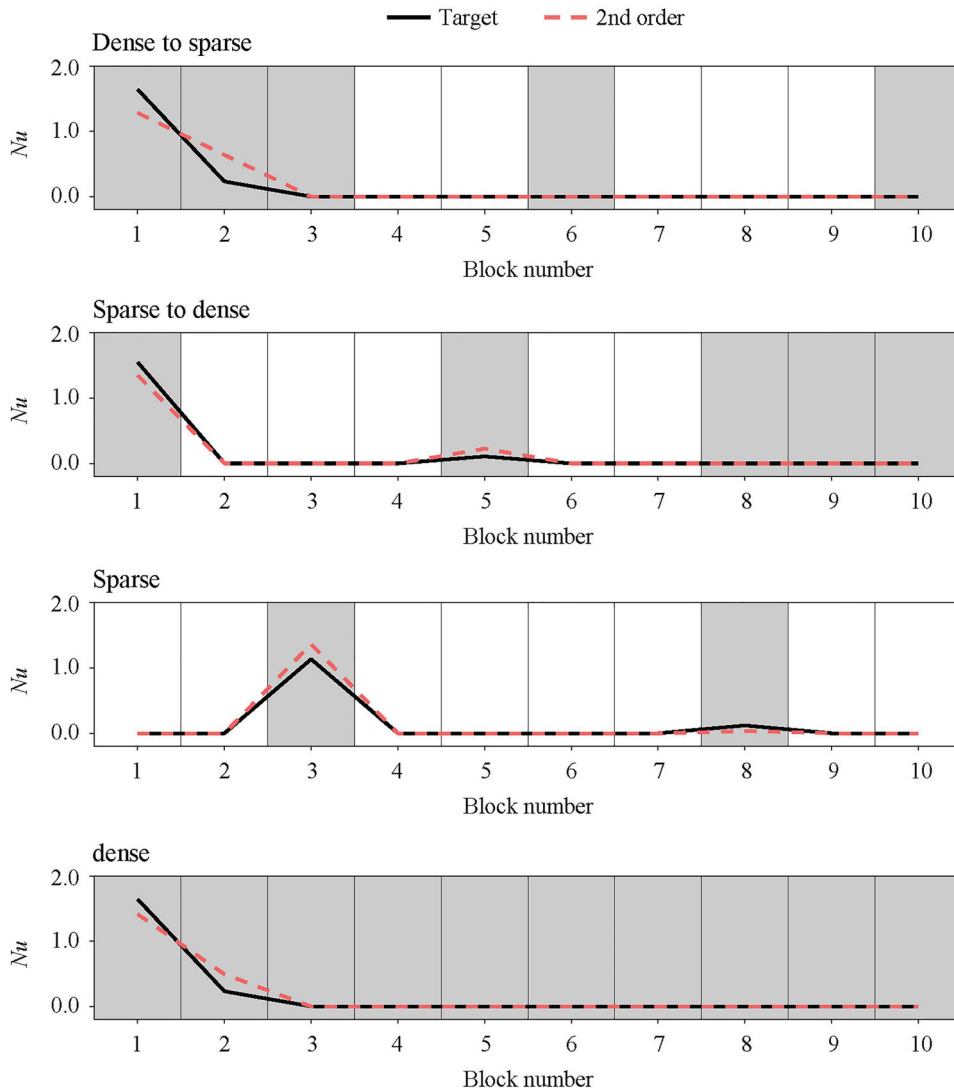

Figure 14. Predicted data of Nu obtained using the second-order approach (red) are compared to the target data (black) in four different cylinder arrays at $Re = 1$.

and 100. To compare the overall performance with previous observations for the representative geometry (see Figure 12), we calculated the mean L_2 error for each characteristic geometric configuration at $Re = 1$ (blue), $Re = 10$ (red), and $Re = 100$ (green) in Figure 17. Our results demonstrate that even with a small number of data layers (e.g. two layers), the mean L_2 error converged to sufficiently small values for $Re = 1$ and $Re = 10$. Additionally, for $Re = 100$, we observed that increasing the number of data layers (i.e. approximately five layers) resulted in excellent performance for all test cases, as indicated by sufficiently small mean L_2 error (< 0.05). From the results, as previously noted in the last section, the L_2 errors were found to be generally higher for higher Reynolds numbers, while the second-order approach demonstrated a robust prediction capability, regardless of the geometric configuration, by consistently showing

a clear trend of decreasing L_2 with an increasing number of training data layers.

3.3. Generalisation for flow regimes

The prediction capability and robustness of the second-order approach were found to extend up to flow regimes with untrained Reynolds numbers whose values were between the trained Reynolds numbers of 1, 10, and 100. Except for the addition of the prediction target of the Reynolds number as an input variable, the training and prediction procedures for the untrained Reynolds number were identical to those used previously. Using data from the trained Reynolds numbers of 1, 10, and 100, the second-order was used to predict the flow and temperature distributions at four different untrained Reynolds numbers of 5, 30, 50, and 70. These predictions were
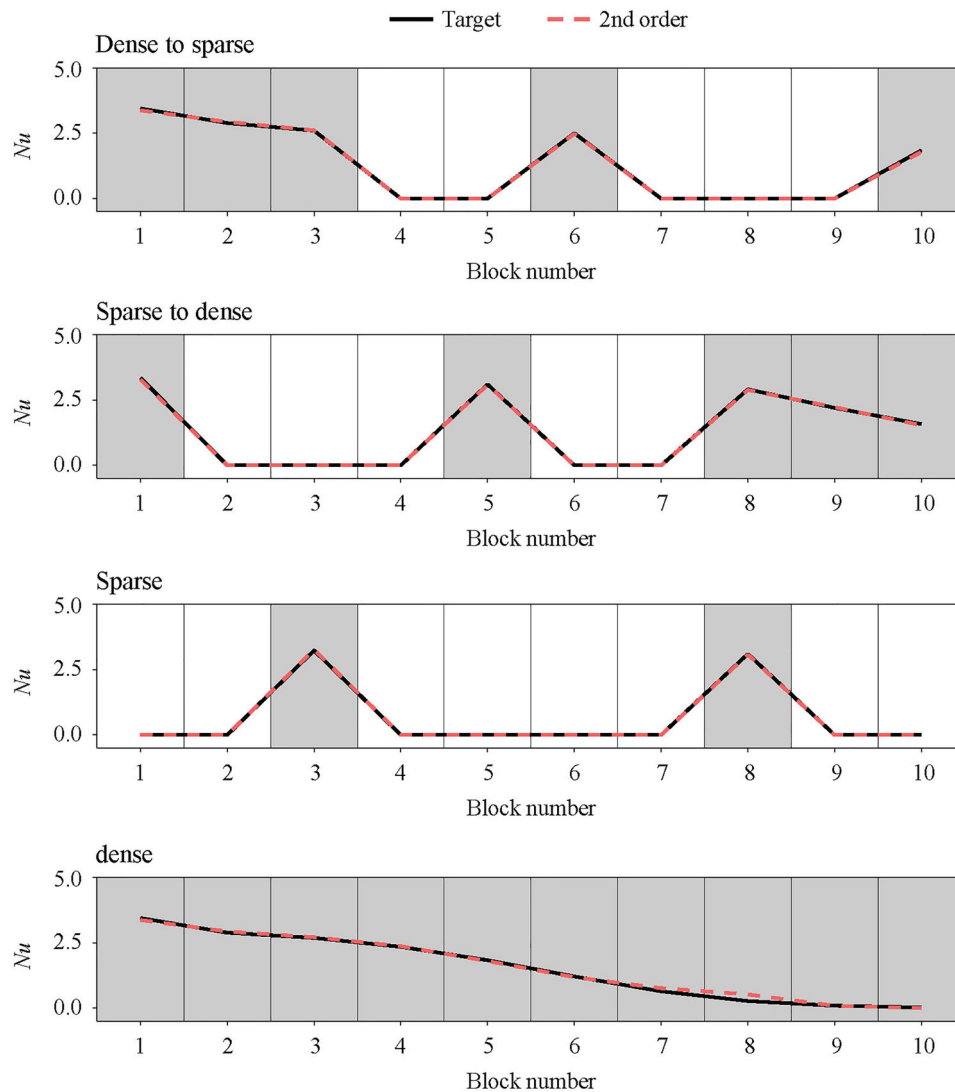

Figure 15. Predicted data of *Nu* obtained using the second-order approach (red) are compared to the target data (black) in four different cylinder arrays at $Re = 10$.
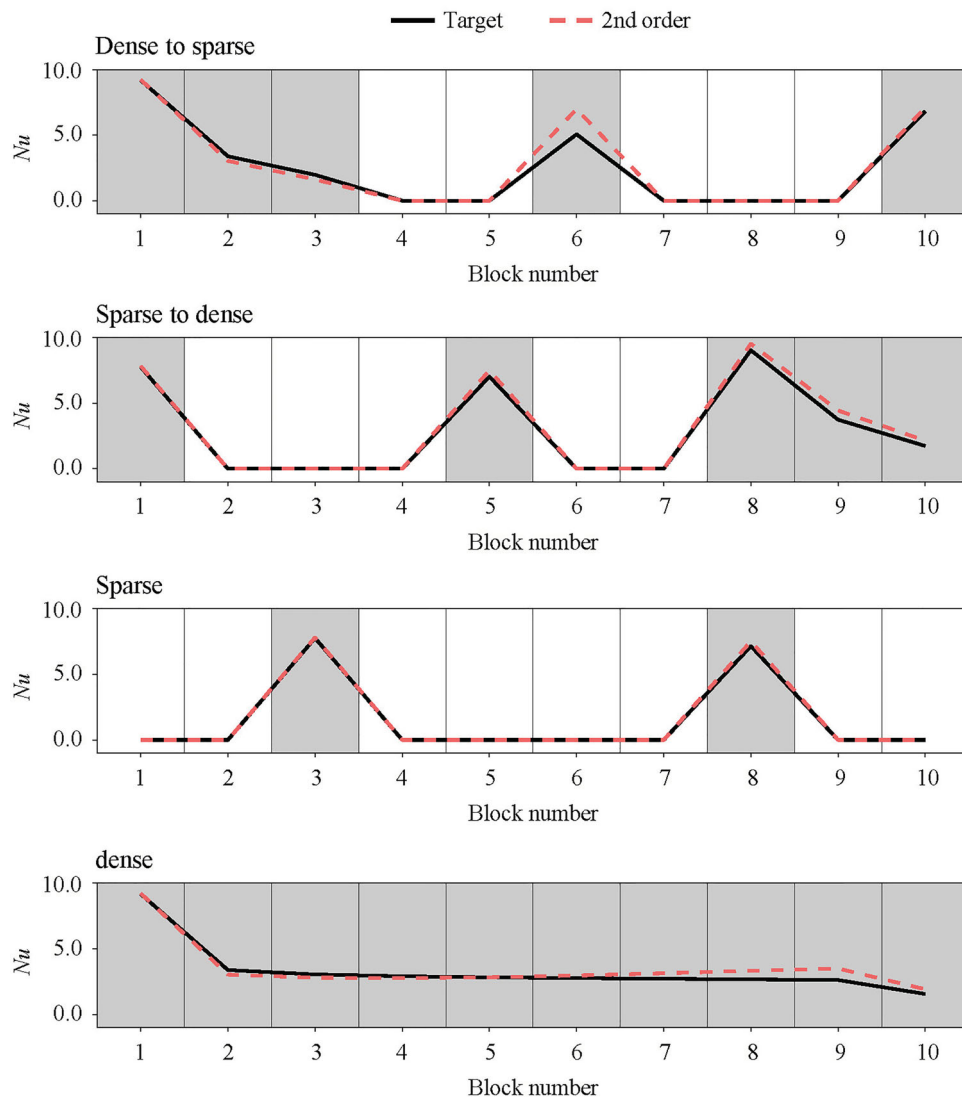
Figure 16. Predicted data of *Nu* obtained using the second-order approach (red) are compared to the target data (black) in four different cylinder arrays at $Re = 100$.

made for five representative cylinder arrays with irregular, dense to sparse, sparse to dense, sparse, and dense configurations, as shown in Figures 4–17. The prediction performance for the untrained Reynolds numbers is shown in Figure 18, which shows the colour map of the prediction error of the mean L_2 versus the number of the training data layer (*x*-axis) and the Reynolds number (*y*-axis). The trained Reynolds numbers of 1, 10, and 100 are coloured magenta on the *y*-axis to distinguish them from the other untrained Reynolds numbers. Figure 18 shows that the mean L_2 errors consistently decrease to < 0.1 with an increasing number of training data layers of up to eight for all flow regimes and geometric configurations. This demonstrates the performance of the present second-order approach in describing the flow and temperature distributions even for untrained data

regimes, by interpolating the flow and temperature characteristics from the trained data regimes. Among the five representative array configurations, the dense array was observed to have the lowest prediction error (darker blue) because the diversity of the flow patterns was relatively limited in this geometry. In addition to the mean L_2 error, additional prediction results for the untrained Reynolds numbers are available in the Supplementary material.

4. Conclusions and future work

The design of well-optimised cylinder arrays is important in thermal and fluid engineering applications, including heat exchangers. Previous studies examined a limited range of geometric configurations with constant spacing, and their findings or correlations rarely encompassed
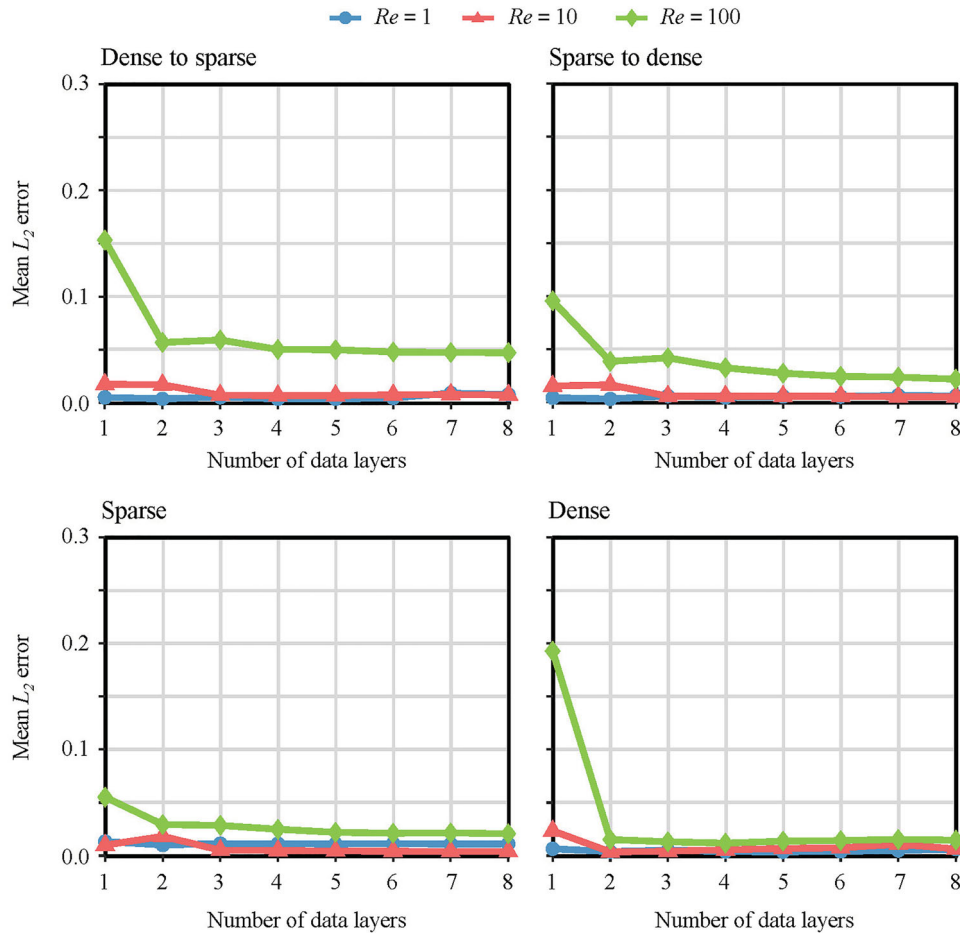
Figure 17. The mean L_2 errors are plotted in four different cylinder arrays at $Re = 1$ (blue), $Re = 10$ (red), and $Re = 100$ (green).

comprehensive general geometries with random arrangements. In this study, we proposed the FLBB approach as a novel methodology for the optimal design of cylinder arrays with random pitch distances in the field of thermal and fluid engineering. We conducted a feasibility study utilising the FLBB to predict the heat transfer and flow characteristics across an in-line cylinder array of the same size with random pitch distances for air ($Pr = 0.71$). This study focused on low Reynolds flow applicable to submicro- to millimetre-scaled applications, such as microchannel heat sinks and hollow fibre membranes. We aimed to establish a correlation to predict the overall heat transfer and pressure drop for such systems, which can be ideal for the initial system design assessment. This preliminary analysis also aimed to assess the capability of the FLBB to accurately capture the thermal and fluid dynamics behaviour in such configurations.

The FLBB is motivated by the classical computational cell, also called a mesh or grid, which has been utilised as a discretizing unit for solving nonlinear mechanical problems numerically. The correlations between the inlet and outlet flow data (velocity, temperature, and pressure drop in this study) were devised using NN-based

regression analysis on systematically organised flow data. Although we obtained impressive results, it is worthwhile to explore alternative regression techniques, including support vector regression (SVR), which is a kernel-based approach (Brunton et al., 2020). Conducting a comparative analysis of the regression performance between the current NN-based regression, SVR and other techniques would yield valuable insights. However, because the primary focus of this study was to introduce the novel concept of FLBB using a simple NN-based regression analysis, we did not conduct an exhaustive analysis of various ML techniques. In the future, we will conduct more comprehensive analyses. For the systematic generation of the training data set, a recursive data generation procedure was proposed where outlet conditions were recursively used as inlet conditions for the next layer. By using such a recursive procedure, the bias in data collection can be minimised, and all possible flow patterns can be covered systematically and effectively without testing an unaffordable number of geometric configurations. Furthermore, the high-order FLBB was employed to tackle strong spatial inter-dependency, especially in high Reynolds number flows where the dynamic vortex-solid
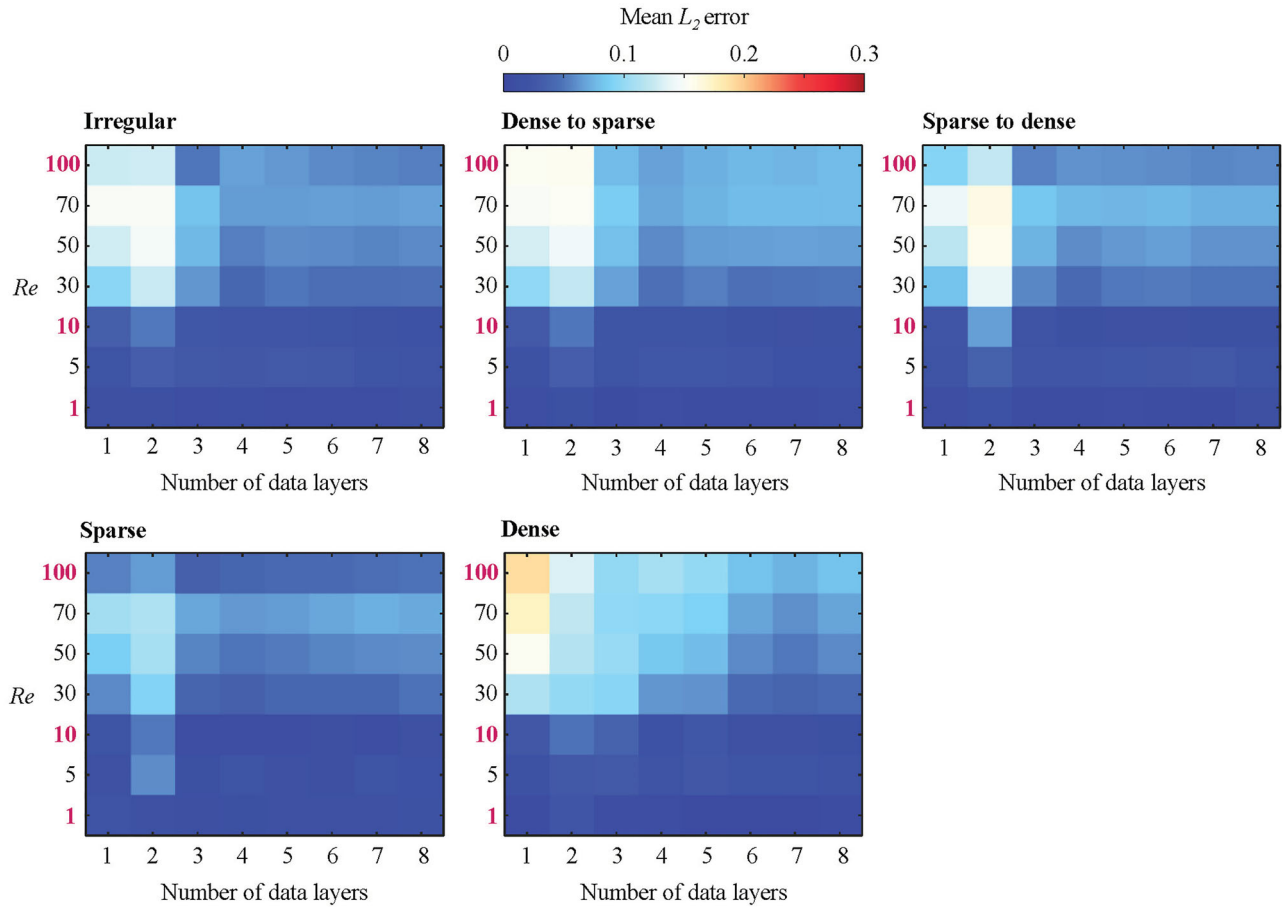
Figure 18. Predictions for the flow regimes at untrained Reynolds numbers based on the second-order FLBB. Colour maps of the mean L_2 error versus Reynolds number (x-axis) and the number of training data layers (y-axis) for five different characteristic cylinder arrays. On the y-axis, the numbers in magenta indicate the trained Reynolds number while the numbers in black represent the untrained Reynolds number to be predicted.

interaction is significant. The prediction robustness of the second-order approach was superior to that of the first-order approach, even for untrained flow regimes when their Reynolds numbers are within the trained Reynolds numbers.

The proposed FLBB is believed to be valuable as a novel approach that is directly applicable to engineering fields. We hope that the proposed general correlation can replace the conventional correlations that are widely used for optimal geometry selection (i.e. pitch distance) of homogeneous array structures. Our procedure enables the evaluation of local behaviours that are typically unobtainable through traditional correlations, which only provide a global picture of the flow behaviour. This allows the detection of flow defects at a local level, such as a high pressure or temperature drop, and thus supports the development of optimally designed cylinder arrays. The scope of the current FLBB is expected to be broadened by including more functions. Importantly, a reinforced ML

model should be embedded in the present FLBB to derive an optimal structural arrangement for each engineering purpose (e.g. highest heat transfer performance) rather than being limited to predicting flow and temperature distributions through a cylinder array. To derive such an optimal structural arrangement, a staggered arrangement of the cylinder array and volume fraction of the cylinder compared with the building box (i.e. the transverse size of the block) should be included in the FLBB in the future. Because the purpose of this study was to introduce the fundamental concept of the FLBB, we only focused on an in-line cylinder array with a fixed diameter, which is the most basic configuration of a cylinder array in fluid engineering. Along with the in-line array, a staggered array is also widely used in heat exchangers, which is known to provide a higher heat transfer rate than the in-line array, but is accompanied by an equivalent increase in the pressure drop as a trade-off (Che & Elbel, 2021; Li et al., 2016). Thus, in a follow-up study to derive an optimal

cylinder array through reinforcement learning, a staggered arrangement will be included owing to its effect on the application performance, such as the heat-transfer rate and pressure drop. Furthermore, introducing other shapes such as elliptical and square cylinder with variance of its angle (Nayak et al., 2019; Yu et al., 2023) can derive more general shape optimisation. While the current research has focused mainly on lower Prandtl numbers, specifically airflow, it should be extended to include higher Prandtl number cases (i.e. water) as well as various other properties, such as viscosity and thermal diffusivity. In addition, the solid fraction of a cylinder in a block and its shape will be considered in the future for further optimisation.

The proposed FLBB provided accurate predictions for heterogeneous and homogeneous cylinder arrays at Reynolds numbers ranging from 1 to 100, including untrained Reynolds numbers. For higher Reynolds numbers, the turbulence should be considered (Gorman et al., 2019). However, at higher Reynolds numbers > 100, it is somewhat difficult to obtain stable solutions of the flow and temperature profiles through a cylinder array with the present CFD code, which is not specialised for turbulent modelling (Gorman et al., 2019). The direct numerical simulation (DNS) or large eddy simulation (LES) of the turbulent flow can be considered to obtain an accurate solution for the ML model. However, because the DNS or LES of the turbulent flow requires considerable computational resources, the computation for the second-order approach with eight-layer dataset, which totals 1,020 different simulations, will be very expensive. In addition, because the current FLBB was designed to be computationally efficient, we focused on the flow regime of $Re \leq 100$, where the flow can be computed precisely without the use of a specialised turbulent model (Gunzburger, 2012). However, future work will extend the FLBB to cover turbulent flow regimes by employing a reliable 3D turbulent model along with a transient effect for training the building blocks.

Acknowledgements

Disclosure statement

Funding

Supplementary material

See the supplementary material for more prediction results.

ORCID

Seungwon Shin http://orcid.org/0000-0002-9196-3966

References

Acharya, M. S., Armaan, A., & Antony, A. S. (2019). A comparison of regression models for prediction of graduate admissions. In *2019 International conference on computational intelligence in data science* (pp. 1–5). IEEE.

Adams, J. C., Swarztrauber, P. N., & Sweet, R.. (2016). FISHPACK90: Efficient fortran subprograms for the solution of separable elliptic partial differential equations. *Astrophysics Source Code Library* (ascl: 1609.004) [Source code]. https://github.com/NCAR/NCAR-Classic-Libraries-for-Geophysics/tree/main/FishPack_90

Araujo, A. D., Andrade, J. S., Jr., & Herrmann, H. J. (2006). Critical role of gravity in filters. *Physical Review Letters*, *97*(13), 138001. https://doi.org/10.1103/PhysRevLett.97.138001

Baranyi, L., & Lewis, R. I. (2006). Comparison of a grid-based CFD method and vortex dynamics predictions of low Reynolds number cylinder flows. *The Aeronautical Journal*, *110*(1103), 63–71. https://doi.org/10.1017/S0001924000004371

Barkley, D., & Henderson, R. D. (1996). Three-dimensional Floquet stability analysis of the wake of a circular cylinder. *Journal of Fluid Mechanics*, *322*, 215–241. https://doi.org/10.1017/S0022112096002777

Bhuiyan, A. A., & Islam, A. S. (2016). Thermal and hydraulic performance of finned-tube heat exchangers under different flow ranges: A review on modeling and experiment. *International Journal of Heat and Mass Transfer*, *101*, 38–59. https://doi.org/10.1016/j.ijheatmasstransfer.2016.05.022

Brunton, S. L., Noack, B. R., & Koumoutsakos, P. (2020). Machine learning for fluid mechanics. *Annual Review of Fluid Mechanics*, *52*(1), 477–508. https://doi.org/10.1146/annurev-fluid-010719-060214

Buda, M., Maki, A., & Mazurowski, M. A. (2018). A systematic study of the class imbalance problem in convolutional neural networks. *Neural Networks*, *106*, 249–259. https://doi.org/10.1016/j.neunet.2018.07.011

Che, M., & Elbel, S. (2021). Experimental quantification of air-side row-by-row heat transfer coefficients on fin-and-tube heat exchangers. *International Journal of Refrigeration*, *131*, 657–665. https://doi.org/10.1016/j.ijrefrig.2021.06.012

Chen, X., & Papathanasiou, T. D. (2008). The transverse permeability of disordered fiber arrays: A statistical correlation in terms of the mean nearest interfiber spacing. *Transport in*

Porous Media, *71*(2), 233–251. https://doi.org/10.1007/s1124 2-007-9123-6

Chew, A. W. Z., & Law, A. W. K. (2019). Feature engineering using homogenization theory with multiscale perturbation analysis for supervised model-based learning of physical clogging condition in seepage filters. *Journal of Computational Science*, *32*, 21–35. https://doi.org/10.1016/j.jocs.2019. 02.003

Chollet, F. (2018). Keras: The python deep learning library. *Astrophysics Source Code Library* (ascl: 1806.022) [Source code]. https://keras.io/

Chorin, A. J. (1968). Numerical solution of the Navier-stokes equations. *Mathematics of Computation*, *22*(104), 745–762. https://doi.org/10.1090/S0025-5718-1968-0242 392-2

Cindrella, L., Kannan, A. M., Lin, J., Saminathan, K., Ho, Y., Lin, C., & Wertz, J. (2009). Gas diffusion layer for proton exchange membrane fuel cells—A review. *Journal of Power Sources*, *194*(1), 146–160. https://doi.org/10.1016/j.jpowsour. 2009.04.005

Colburn, A. P. (1993). A method for correlating forced convection heat transfer data and a comparison with fluid friction. *Transfer AIChE*, *29*, 174–210.

da Silva, B. L., Luciano, R. D., Utzig, J., & Meier, H. F. (2018). Flow patterns and turbulence effects in large cylinder arrays. *International Journal of Heat and Fluid Flow*, *69*, 136–149. https://doi.org/10.1016/j.ijheatfluidflow.2017.12.013

Dhar, B., Mahapatra, S., Maharana, S., Sarkar, A., & Sahoo, S. (2016). Numerical study on phase change of water flowing across two heated rotating circular cylinders in tandem arrangement. *The Journal of Computational Multiphase Flows*, *8*(4), 201–212. https://doi.org/10.1177/1757482X166 74218

Dhar, B., Mahapatra, S., Maharana, S., Sarkar, A., & Sahoo, S. (2017). Numerical study on phase change of water flowing across two heated circular cylinders in tandem arrangement. *Heat Transfer—Asian Research*, *46*(7), 656–680. https://doi.org/10.1002/htj.21236

Duraisamy, K., Iaccarino, G., & Xiao, H. (2019). Turbulence modeling in the age of data. *Annual Review of Fluid Mechanics*, *51*(1), 357–377. https://doi.org/10.1146/annurev-fluid-010518-040547

Estabrooks, A., Jo, T., & Japkowicz, N. (2004). A multiple resampling method for learning from imbalanced data sets. *Computational Intelligence*, *20*(1), 18–36. https://doi.org/10. 1111/j.0824-7935.2004.t01-1-00228.x

Faghri, A., & Zhang, Y. (2006). *Transport phenomena in multiphase systems*. Elsevier.

Ferziger, J. H., & Peric, M. (2002). *Computational methods for fluid dynamics*. Springer.

Ge, Y., Lin, Y., Tao, S., He, Q., Chen, B., & Huang, S.-M. (2021). Shape optimization for a tube bank based on the numerical simulation and multi-objective genetic algorithm. *International Journal of Thermal Sciences*, *161*, 106787. https://doi.org/10.1016/j.ijthermalsci.2020.106787

Gorman, J. M., Sparrow, E. M., & Ahn, J. (2019). In-line tube-bank heat exchangers: Arrays with various numbers of thermally participating tubes. *International Journal of Heat and Mass Transfer*, *132*, 837–847. https://doi.org/10.1016/j.ijheat masstransfer.2018.11.167

Grimison, E. (1937). Correlation and utilization of new data on flow resistance and heat transfer for cross flow of gases over tube banks. *Transactions of the American Society of Mechanical Engineers*, *59*(7), 583–594.

Gunzburger, M. D. (2012). *Finite element methods for viscous incompressible flows: A guide to theory, practice, and algorithms*. Elsevier.

Halkarni, S. S., Sridharan, A., & Prabhu, S. V. (2017). Measurement of local wall heat transfer coefficient in randomly packed beds of uniform sized spheres using infrared thermography (IR) and water as working medium. *Applied Thermal Engineering*, *126*, 358–378. https://doi.org/10.1016/j.ap plthermaleng.2017.07.174

Han, R., Wang, Y., Qian, W., Wang, W., Zhang, M., & Chen, G. (2022). Deep neural network based reduced-order model for fluid–structure interaction system. *Physics of Fluids*, *34*(7), 073610. https://doi.org/10.1063/5.0096432

Harlow, F. H., & Welch, J. E. (1965). Numerical calculation of time-dependent viscous incompressible flow of fluid with free surface. *The Physics of Fluids*, *8*(12), 2182–2189. https://doi.org/10.1063/1.1761178

Hasan, M. I. (2014). Investigation of flow and heat transfer characteristics in micro pin fin heat sink with nanofluid. *Applied Thermal Engineering*, *63*(2), 598–607. https://doi.org /10.1016/j.applthermaleng.2013.11.059

He, H., & Garcia, E. A. (2009). Learning from imbalanced data. *IEEE Transactions on Knowledge and Data Engineering*, *21*(9), 1263–1284. https://doi.org/10.1109/TKDE.2008.239

He, K., & Zhang, L.-Z. (2020). Cross flow and heat transfer of hollow-fiber tube banks with complex distribution patterns and various baffle designs. *International Journal of Heat and Mass Transfer*, *147*, 118937. https://doi.org/10.1016/j.ijheat masstransfer.2019.118937

Henderson, R. D. (1997). Nonlinear dynamics and pattern formation in turbulent wake transition. *Journal of Fluid Mechanics*, *352*, 65–112. https://doi.org/10.1017/S00221120 97007465

Herwig, H., & Mahulikar, S. P. (2006). Variable property effects in single-phase incompressible flows through microchannels. *International Journal of Thermal Sciences*, *45*(10), 977–981. https://doi.org/10.1016/j.ijthermalsci.2006.01.002

Hornik, K., Stinchcombe, M., & White, H. (1989). Multilayer feedforward networks are universal approximators. *Neural Networks*, *2*(5), 359–366. https://doi.org/10.1016/0893-6080 (89)90020-8

IEEE Standards Board. (1990). *IEEE standard glossary of software engineering terminology (610.12-1990)*. IEEE.

Incropera, F. P., DeWitt, D. P., Bergman, T. L., & Lavine, A. S. (1996). *Fundamentals of heat and mass transfer*. Wiley.

Jiang, R., Yang, M., Chen, S., Huang, S.-M., & Yang, X. (2014). Fluid flow and heat transfer across an elliptical hollow fiber membrane tube bank with randomly distributed features. *International Journal of Heat and Mass Transfer*, *76*, 559–567. https://doi.org/10.1016/j.ijheatmasstransfer.2014.05.004

Jin, X., Cai, S., Li, H., & Karniadakis, G. E. (2021). NSFnets (Navier-Stokes flow nets): Physics-informed neural networks for the incompressible Navier-Stokes equations. *Journal of Computational Physics*, *426*, 109951. https://doi.org/ 10.1016/j.jcp.2020.109951

Jin, X., Cheng, P., Chen, W.-L., & Li, H. (2018). Prediction model of velocity field around circular cylinder over various Reynolds numbers by fusion convolutional neural networks based on pressure on the cylinder. *Physics of Fluids*, *30*(4), 047105. https://doi.org/10.1063/1.5024595

Khan, W. A., Culham, J. R., & Yovanovich, M. M. (2006). Convection heat transfer from tube banks in crossflow: Analytical approach. *International Journal of Heat and Mass Transfer*, *49*(25–26), 4831–4838. https://doi.org/10.1016/j.ijheatmasstransfer.2006.05.042

Kingma, D. P., & Ba, J. (2014). Adam: A method for stochastic optimization. *arXiv preprint arXiv:1412.6980*.

Krizhevsky, A., Sutskever, I., & Hinton, G. E. (2012). ImageNet classification with deep convolutional neural networks. *Advances in Neural Information Processing Systems*, *25*, 1097–1105.

Kutz, J. N., Brunton, S. L., Brunton, B. W., & Proctor, J. L. (2016). *Dynamic mode decomposition: Data-driven modeling of complex systems*. SIAM.

Lee, D., Ahn, J., & Shin, S. (2013). Uneven longitudinal pitch effect on tube bank heat transfer in cross flow. *Applied Thermal Engineering*, *51*(1–2), 937–947. https://doi.org/10.1016/j.applthermaleng.2012.10.031

Lee, S., & You, D. (2019). Data-driven prediction of unsteady flow over a circular cylinder using deep learning. *Journal of Fluid Mechanics*, *879*, 217–254. https://doi.org/10.1017/jfm.2019.700

Li, W., Shen, S., & Li, H. (2016). Study and optimization of the filtration performance of multi–fiber filter. *Advanced Powder Technology*, *27*(2), 638–645. https://doi.org/10.1016/j.apt.2016.02.018

Ling, J., Kurzawski, A., & Templeton, J. (2016). Reynolds averaged turbulence modelling using deep neural networks with embedded invariance. *Journal of Fluid Mechanics*, *807*, 155–166. https://doi.org/10.1017/jfm.2016.615

Maulud, D., & Abdulazeez, A. M. (2020). A review on linear regression comprehensive in machine learning. *Journal of Applied Science and Technology Trends*, *1*(4), 140–147. https://doi.org/10.38094/jastt1457

Meneghini, J. R., Saltara, F., Siqueira, C. L. R., & Ferrari, J., Jr. (2001). Numerical simulation of flow interference between two circular cylinders in tandem and side-by-side arrangements. *Journal of Fluids and Structures*, *15*(2), 327–350. https://doi.org/10.1006/jfls.2000.0343

Munson, B. R., Okiishi, T. H., Huebsch, W. W., & Rothmayer, A. P. (2013). *Fluid mechanics*. Wiley Singapore.

Nayak, R. K., Ray, S., Sahoo, S. S., & Satapathy, P. K. (2019). Effect of angle of attack and wind direction on limiting input heat flux for solar assisted thermoelectric power generator with plate fin heat sink. *Solar Energy*, *186*, 175–190. https://doi.org/10.1016/j.solener.2019.05.010

Nemec, D., & Levec, J. (2005). Flow through packed bed reactors: 1. Single-phase flow. *Chemical Engineering Science*, *60*(24), 6947–6957. https://doi.org/10.1016/j.ces.2005.05.068

Noorman, S., van Sint Annaland, M., & Kuipers, H. (2007). Packed bed reactor technology for chemical-looping combustion. *Industrial & Engineering Chemistry Research*, *46*(12), 4212–4220. https://doi.org/10.1021/ie061178i

Printsypar, G., Bruna, M., & Griffiths, I. M. (2018). The influence of porous-medium microstructure on filtration. *Journal of Fluid Mechanics*, *861*, 484–516. https://doi.org/10.1017/jfm.2018.875

Raissi, M., Perdikaris, P., & Karniadakis, G. E. (2017). Physics informed deep learning (part i): Data-driven solutions of nonlinear partial differential equations. *arXiv preprint arXiv:1711.10561*.

Raissi, M., Perdikaris, P., & Karniadakis, G. E. (2019). Physics-informed neural networks: A deep learning framework for solving forward and inverse problems involving nonlinear partial differential equations. *Journal of Computational Physics*, *378*, 686–707. https://doi.org/10.1016/j.jcp.2018.10.045

Raissi, M., Yazdani, A., & Karniadakis, G. E. (2020). Hidden fluid mechanics: Learning velocity and pressure fields from flow visualizations. *Science*, *367*(6481), 1026–1030. https://doi.org/10.1126/science.aaw4741

Rastan, M. R., Sohankar, A., & Alam, M. M. (2021). Flow and heat transfer across two inline rotating cylinders: Effects of blockage, gap spacing, Reynolds number, and rotation direction. *International Journal of Heat and Mass Transfer*, *174*, 121324. https://doi.org/10.1016/j.ijheatmasstransfer.2021.121324

Schmid, P. J. (2010). Dynamic mode decomposition of numerical and experimental data. *Journal of Fluid Mechanics*, *656*, 5–28. https://doi.org/10.1017/S0022112010001217

Sharman, B., Lien, F. S., Davidson, L., & Norberg, C. (2005). Numerical predictions of low Reynolds number flows over two tandem circular cylinders. *International Journal for Numerical Methods in Fluids*, *47*(5), 423–447. https://doi.org/10.1002/fld.812

Shu, C.-W., & Osher, S. (1988). Efficient implementation of essentially non-oscillatory shock-capturing schemes. *Journal of Computational Physics*, *77*(2), 439–471. https://doi.org/10.1016/0021-9991(88)90177-5

Sumner, D. (2010). Two circular cylinders in cross-flow: A review. *Journal of Fluids and Structures*, *26*(6), 849–899. https://doi.org/10.1016/j.jfluidstructs.2010.07.001

Tamayol, A., & Bahrami, M. (2011). Water permeation through gas diffusion layers of proton exchange membrane fuel cells. *Journal of Power Sources*, *196*(15), 6356–6361. https://doi.org/10.1016/j.jpowsour.2011.02.069

Tseng, Y.-H., & Ferziger, J. H. (2003). A ghost-cell immersed boundary method for flow in complex geometry. *Journal of Computational Physics*, *192*(2), 593–623. https://doi.org/10.1016/j.jcp.2003.07.024

Wang, J.-X., Wu, J.-L., & Xiao, H. (2017). Physics-informed machine learning approach for reconstructing Reynolds stress modeling discrepancies based on DNS data. *Physical Review Fluids*, *2*(3), 034603. https://doi.org/10.1103/PhysRevFluids.2.034603

Wang, X., & Sun, X. (2016). An improved weighted naive bayesian classification algorithm based on multivariable linear regression model. In *2016 9th International symposium on computational intelligence and design* (pp. 219–222). IEEE.

Williams, M. V., Begg, E., Bonville, L., Kunz, H. R., & Fenton, J. M. (2004). Characterization of gas diffusion layers for PEMFC. *Journal of the Electrochemical Society*, *151*(8), A1173. https://doi.org/10.1149/1.1764779

Wu, P., Sun, J., Chang, X., Zhang, W., Arcucci, R., Guo, Y., & Pain, C. C. (2020). Data-driven reduced order model with temporal convolutional neural network. *Computer Methods in Applied Mechanics and Engineering*, *360*, 112766. https://doi.org/10.1016/j.cma.2019.112766

Xu, H., & Mannor, S. (2012). Robustness and generalization. *Machine Learning*, *86*(3), 391–423. https://doi.org/10.1007/s10994-011-5268-1

Yu, C., Zhu, X., Li, Z., Ma, Y., Yang, M., & Zhang, H. (2023). Optimization of elliptical pin-fin microchannel heat sink based on artificial neural network. *International Journal of Heat and Mass Transfer*, *205*, 123928. https://doi.org/10.1016/j.ijheatmasstransfer.2023.123928

Zargartalebi, M., & Azaiez, J. (2019). Flow dynamics and heat transfer in partially porous microchannel heat sinks. *Journal of Fluid Mechanics*, *875*, 1035–1057. https://doi.org/10.1017/jfm.2019.491

Zargartalebi, M., Benneker, A. M., & Azaiez, J. (2020). The impact of heterogeneous pin based micro-structures on flow dynamics and heat transfer in micro-scale heat exchangers. *Physics of Fluids*, *32*(5), 052007. https://doi.org/10.1063/5.0006577

Zhang, X., Ji, T., Xie, F., Zheng, C., & Zheng, Y. (2022). Data-driven nonlinear reduced-order modeling of unsteady fluid–structure interactions. *Physics of Fluids*, *34*(5), 053608. https://doi.org/10.1063/5.0090394

Zhang, Z., Li, Y., Li, L., Li, Z., & Liu, S. (2019). Multiple linear regression for high efficiency video intra coding. In *ICASSP 2019–2019 IEEE international conference on acoustics, speech and signal processing* (pp. 1832–1836). IEEE.

Zhou, Z., He, G., Wang, S., & Jin, G. (2019). Subgrid-scale model for large-eddy simulation of isotropic turbulent flows using an artificial neural network. *Computers & Fluids*, *195*, 104319. https://doi.org/10.1016/j.compfluid.2019.104319

Zukauskas, A., & Ulinskas, R. (1988). *Heat transfer in tube banks in crossflow*. Springer.